

Degree in Biomedical Engineering
2022-2023

Bachelor Thesis

“Omnipole Limitations in High Density Multielectrode Catheters: A Comparative Study on Epicardial Signals”

Marina Crespo Aguirre

Manuel Desco Menéndez

José Millet Roig

Francisco Castells

Samuel Ruipérez-Campillo

Madrid, 16th June 2023



This work is licensed under Creative Commons **Attribution – Non Commercial – Non Derivatives**

ABSTRACT

The appearance of new high density multielectrode catheters has given rise to novel standing points in the field of cardiac electrophysiology. In particular, the High Density (HD) Grid from Abbot, with a 4x4 matrix structure of electrodes separated with 3 mm between them, has allowed the creation of a new reconstruction of the Electrogram (EGM) signals, and has given rise to some of the inquiries that have encouraged the development of this dissertation work.

This study aims to determine how distance affects the reconstruction of EGMs, by conducting a comparative study of different omni polar configuration modalities. With inter-electrode distances of 1 to 4 mm, analyzing their effect on the quality of the resulting EGMs. The recordings used in this study were selected from a collection of experimental recordings on perfused isolated rabbit hearts using a high-density epicardial multielectrode catheter. Besides, a reconstruction algorithm is implemented to some signals that present a saturation region related to the method of amplification used.

Computing different biomarkers we are able to identify the areas contained within the bipolar loops and the amplitudes, ratios, morphological distortion, as well as the pulse widths of the omni polar signals. We analyze the results making use of a refined statistical model, adapted to the characteristics of our dataset.

The hypothesis sustained along this work is that at shorter inter-electrode distances, both Bipolar Electrogram (bEGM)s and Omnipolar Electrogram (oEGM)s are more robust, with loops aligned with the propagation direction and omnipoles clearly illustrating the activation time point. The results retrieved support our hypothesis, and provide a more robust estimation method of the wavefront propagation, the cross-omnipolar reconstruction arrangement.

* Key Concepts

Multielectrode catheter: Specialized medical device designed to record the electrical signals within the heart and to create a detailed map of its electrical activity. Commonly inserted through a blood vessel and positioned into the heart, the electrode leads of the device record the electric signals of the cavity under study.

Electrogram: Recording of the electrical activity within the heart. Represented as the electrical waveform over time, it provides detailed information about depolarization events taking place in the myocardial tissue.

Cardiac Ablation: Medical procedure based on scarring abnormal myocardial tissue responsible for arrhythmias. A catheter inserted through a blood vessel, delivers radio-frequency energy to targeted areas, with the purpose of recovering the normal heart rhythm.

ACRONYMS

A-V Atrio-Ventricular. 5, 8–10, 13	OA Omnipolar Amplitude. vii, 28, 31, 32, 34, 38, 39, 45
AF Atrial Fibrillation. 16, 17, 51	OD Omnipolar Distortion. vii, 29, 30, 32, 34, 38, 39, 45
AP Action Potential. 7, 8	oEGM Omnipolar Electrogram. iii, vii, x, 1, 23, 24, 26, 28–30, 34, 35, 38, 42, 43, 46–48
bEGM Bipolar Electrogram. iii, vii, 16, 20, 22, 23, 28, 29, 34, 38, 41, 46–48	OR Omnipolar Ratio. vii, 28, 31, 32, 34, 38, 39, 45
CFAE Complex Fractionated Electrogram. 17	OW Omnipolar Width. vii, 29, 32, 34, 38, 39, 45
CV Conduction Velocity. 17	RA Right Atrium. 5–7
ECG Electrocardiogram. 9, 11–14	RV Right Ventricle. 5, 6
ECM Extracellular Matrix. 14	SA Sinoatrial. 6, 8, 13
EGM Electrogram. iii, 1, 16, 17, 19, 23, 34	SCD Sudden Cardiac Death. 51
HD High Density. iii, x, 1, 17, 18, 47	uEGM Unipolar Electrogram. 16, 17, 21, 24–27, 29, 46
LA Left Atrium. 5, 6	VF Ventricular Fibrillation. 51
LAT Local Activation Time. 17	VT Ventricular Tachycardia. 51
LV Left Ventricle. 5, 6	
LVA Low Voltage Area. 17	
NBA Normalized Bipolar Area. vii, 28, 32, 34, 38, 39, 41, 45	

AGRADECIMIENTOS

Quiero agradecer este trabajo en primer lugar al equipo de investigación de ITACA de Valencia, a los profesores Millet y Castells; no habría logrado esto sin vuestra ayuda, disciplina y exigencia. Gracias por dejarme colaborar con vuestro gran equipo, por creer en mí y confiarne este proyecto del que he aprendido enormemente. También quiero agradecer a Samuel la gran ayuda que me ha prestado desde el principio. Sin tu coaching no habría sabido llegar tan lejos, muchas gracias por tu paciencia, ejemplo y sabiduría. Sigo aprendiendo de ti y estaré encantada de colaborar en más proyectos.

Por otro lado me gustaría agradecerle a mi familia el apoyo y cariño, gracias Papa y Mamá por vuestra enorme paciencia, os quiero.

Entré en la Universidad Carlos III casi recién salida del cascarón, con ansias por aprender y expandir mis conocimientos al máximo. Parece mentira que hayan pasado ya cuatro años, en los que he crecido y me he formado como ingeniera biomédica, pero también como persona. A todos aquellos que habéis puesto vuestro granito de arena en el proceso, en Madrid, en Maryland o donde haya sido, muchas gracias.

CONTENTS

1. INTRODUCTION	1
1.1. Motivation	1
1.2. Objectives and Contribution of the Author	2
1.3. Structure of the Bachelor Thesis	2
2. STATE OF THE ART	4
2.1. The Human Pump	4
2.1.1. Anatomy of the heart	5
2.1.2. Physiology of the heart	6
2.2. Arrhythmogenesis	12
2.3. Cardiac Fibrosis	14
2.3.1. Tissue characterization.	15
3. MATERIALS	19
4. METHODS	20
4.1. Acquisition of the EGM signals.	20
4.2. Computation of the bEGMs	20
4.3. Computation of the oEGM	23
4.3.1. Unipolar reconstruction algorithm	24
4.4. Parameters of assessment of the signals	28
4.4.1. Areas of the bEGMs: NBA	28
4.4.2. Amplitude of the oEGM: OA	28
4.4.3. Ratio of the oEGM: OR	28
4.4.4. Width of oEGM pulse: OW	29
4.4.5. Distortion of the oEGM: OD	29
4.5. Statistical Analysis	32
5. RESULTS	34
5.1. Morphological analysis of a particular signal	34
5.2. Quantitative Analysis	38
5.2.1. Boxplots and statistical analysis	39

5.2.2. Distance effect	42
6. DISCUSSION	46
7. CONCLUSION	48
8. LIMITATIONS AND FUTURE APPROACHES	49
9. REGULATORY FRAMEWORK AND SOCIO-ECONOMICAL IMPACT	50
9.1. Regulatory Frames: Bioethics, Legislation and Licensing	50
9.2. Socio - Economic Impact	51
9.2.1. Socio-Economic Environment	51
9.2.2. Project resources and Costs	52
BIBLIOGRAPHY	54

LIST OF FIGURES

2.1	The heart location	4
2.2	The heart layers	5
2.3	The heart anatomy	6
2.4	The cardiac muscle	7
2.5	Myocardium potential	8
2.6	The heart conduction system	9
2.7	Illustration of the cardiac cycle	10
2.8	Illustration of a heart valve	10
2.9	The ECG	11
2.10	Events associated with one heartbeat	12
2.11	Examples of arrhythmia-induced cardiomyopathies	13
2.12	Bradycardia and Tachycardia	14
2.13	Cardiac Fibrosis	15
2.14	Catheter ablation	16
2.15	Unipolar EGM	17
2.16	Electrode arrangement for EGM recording	17
2.17	Illustration of Advisor ^{TMHD} Grid	18
3.1	Description of the experiment	19
4.1	Acquisition of a uEGM from an electrode channel	20
4.2	Configuration of a clique of electrodes	21
4.3	Example of the electric field loop (in black) with the activation wavefront (in red)	22
4.4	Obtention of the oEGM	23
4.5	Example of the horizontal component (in black) and vertical omnipolar component (in grey)	24
4.6	Saturation of a unipolar signal	24
4.7	Algorithm of reconstruction	25

4.8	Reconstruction of uEGM for different parameters of 'c'	26
4.9	Reconstruction of a clique of saturated uEGMs	27
4.10	Illustration of the metrics	31
5.1	bEGMs from a signal	36
5.2	oEGMs from a particular signal	37
5.3	Boxplots illustrating the results of the parameters of assessment	40
5.4	Morphology Analysis of the omnipoles	43

LIST OF TABLES

5.1	Results for the defined variables of assessment	39
5.2	P-values for the different metrics of assessment, comparing groups to each other	44
5.3	p-values for the metrics of assessment comparing each group class	45
9.1	Human Resources breakdown	52
9.2	Material resources breakdown	52
9.3	Attendance to CASEIB congress	53
9.4	Total cost breakdown	53

1. INTRODUCTION

1.1. Motivation

Cardiac Arrhythmia, defined as any alteration of the heart rhythm, is the cause for the disruption of a heart's regularly synchronized contraction, thus influencing the organ's pumping efficiency [1]. They are in fact an important cause of morbidity and mortality [2], each year more than 300,000 individuals die in the United States suffering from some kind of arrhythmia [3]. Fibrosis plays an important role in inducing arrythmias to persist [4]; in fact, the role of fibrosis in the creation of routes with anomalous conduction within the cardiac substrate, leads to meandering and inhomogeneous electrical activation of the cardiac cells [5]. The examination of the cardiac tissue is therefore highly relevant for the proper characterization of the electrophysiologic substrate. Understanding the mechanisms responsible for cardiac arrhythmias will be the first step to diagnose them and treat them properly.

To date, multiple electroanatomic navigators have been proposed for the electrophysiological characterization of the substrate. More in particular, the High electron Density catheters are increasingly gaining popularity in the field [6]–[8]. The major benefit of these novel catheters when compared to others [9], includes a more accurate estimation of the electrical conduction, linked to the HD mapping of the substrate by means of an array of 4x4 equally distanced electrodes. The potential of these electroanatomic navigators relies on the omnipolar technology they retrieve oEGM [10], a novel orientation-independent biomarker that is able to recreate the hypothetical signal illustrating the direction of wavefront propagation of the local tissue. Nonetheless, there is some underestimation in the robustness of this technology [11] related to a claimed a vulnerability of the oEGM with respect to the relationship of the wavefront propagation direction and the orientation of the pair of electrodes recording the voltage.

This bachelor thesis focuses on the study of oEGM, assessing the effect of different configuration methods on the quality of the reconstructed omnipolar signals, and testing the influence of the inter-electrode distance currently employed in clinical catheters. To do so, an experimental set of isolated perfused rabbit hearts using the Langerdoff technique was employed. Signals were registered by means of a HD multielectrode array of 128 electrodes 1 mm spaced, placed over the epicardiac region of the heart, which was stimulated using a bipolar electrode. Algorithms were proposed to first obtain and then assess the robustness of the EGMs, evaluating the activation amplitude, duration of the pulse and the size of the loops recorded. A statistical model was designed adapted to the data set, to correctly interprete the results and test the hypotheses.

1.2. Objectives and Contribution of the Author

Note that the author of this bachelor dissertation can attribute all merits except for the experimental procedures and the election of the statistical model employed. The main goals to be targeted by this work are summarized below.

- To determine relevant metrics of assessment to test the robustness and accuracy of the physiological biomarkers, as well as a graphical illustration and interpretation of their behavior.
- To design a reconstruction algorithm that recovers the saturated set of unipolar electrograms this study will use.
- To design an adequate statistical model for the correct interpretation of the results.
- To develop a detailed discussion about the results retrieved, together with clear conclusions where the hypothesis are proven, stating the limitations of currently used clinical catheters and proposing future approaches.
- To place the project in the appropriate regulatory framework and socio-economical environment describing costs and impacts.

1.3. Structure of the Bachelor Thesis

This dissertation presents an organized structure with the purpose of clearly exposing the main necessities of the clinical practise to properly diagnose cardiac tissue irregularities and to treat them accordingly.

For this purpose, an extended State of the Art will be given, providing general background on certain concepts that will be fundamental to understand further aspects. From a general understanding of the heart and its role in the circulatory system, I will progressively go deeper into more specific concepts related to the electrical cardiac system, and the methods used to measure the cardiac signals; only to conclude with some heart pathologies and their current treatments. Subsequently, I will briefly expose the Materials section, followed by a detailed exposition of the Methodology followed. The biomarkers employed as well as the different measuring parameters used to assess the quality of the resulting signals will be subject of discussion.

Although the statistical model was not particularly selected by the author of the thesis, an extended description of the model will be provided, together with a thorough explanation of the numerical results and an interpretation of all the graphical illustrations and tables.

The findings from this dissertation work will be exposed in detail in the discussion section, with a clear exposition of the relationship between numerical results and the initial hypothesis.

I will conclude with the main ideas derived from this study, together with the major relevance that this novel reconstruction method represents for the clinical practise. Moreover, some of the limitations we count with in this thesis will be mentioned, which will leave room for future work to be carried out.

To come to an end, the socio-economical and regulatory frames will be equally presented, together with the resources and costs contextualizing this work.

2. STATE OF THE ART

2.1. The Human Pump

The human body strives for balance, the circulatory system being an illustrative example of this statement. Referred to as the transport system of the body [12], the circulatory system is composed of the blood, the channels through which it flows, and the pump that monitors the transport and propels the blood throughout the body; administering oxygen, carbon dioxide, nutrients and hormones to and from cells and ensuring homeostasis is maintained.

Possibly one of the most important organs in the body, the heart lies on the diaphragm, within the thoracic cavity, medially between the lungs and in the mediastinum, the region extending from the sternum to the vertebral column [13], as it can be observed in figure 2.1. It is approximately a closed fist size, isolated and sustained by the pericardium, a membrane that lubricates the moving structures of the heart and that holds it in a fixed position [14].

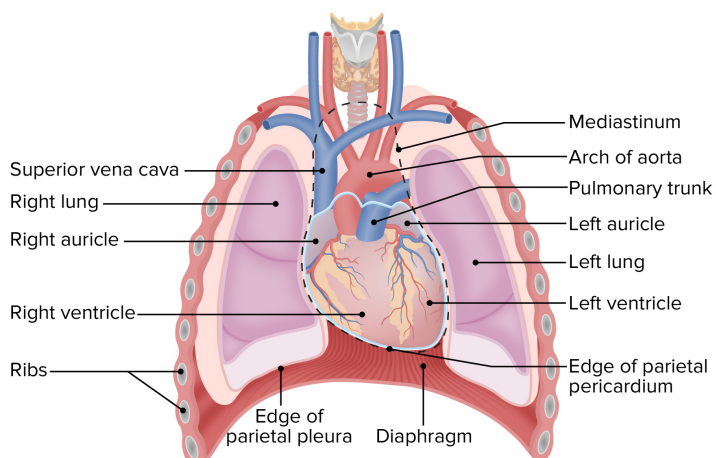


Figure. 2.1. The heart location. Labeled illustration of the placement of the heart within a thoracic cavity (Retrieved from online source).

The pericardium consists of a superficial fibrous layer (parietal pericardium) and a deeper serous layer (serous pericardium) composed of mesothelial cells [15]. The parietal pericardium on the one hand, is the one responsible for the anchoring of the organ to the mediastinum, and it consists of blood vessels entering and leaving the heart to nurture the cells forming the cardiac muscle [16]. The serous pericardium forms a double layer around the heart, which provides the site where the pericardial fluid is found, a lubricating secretion that reduces the friction between layers when the heart is moving [17]. Lastly, the inner part of the serous pericardium is the epicardium.

Composed of three layers (see Figure 2.2), the walls of the heart consist in the epi-

cardium, the myocardium and the endocardium. The epicardium being the external layer, is composed by two sublayers: the visceral serous pericardium and an inner layer that is made of adipous tissue. The myocardium lies underneath, it is nurtured by the blood vessels of the epicardium and it contains the muscle cells responsible for the characteristic pumping of the organ. Lastly, the innermost layer or endocardium, is the endothelial tissue lining the chambers of the heart and covering the valves. This lining decreases the friction generated when blood flows through the heart chambers.

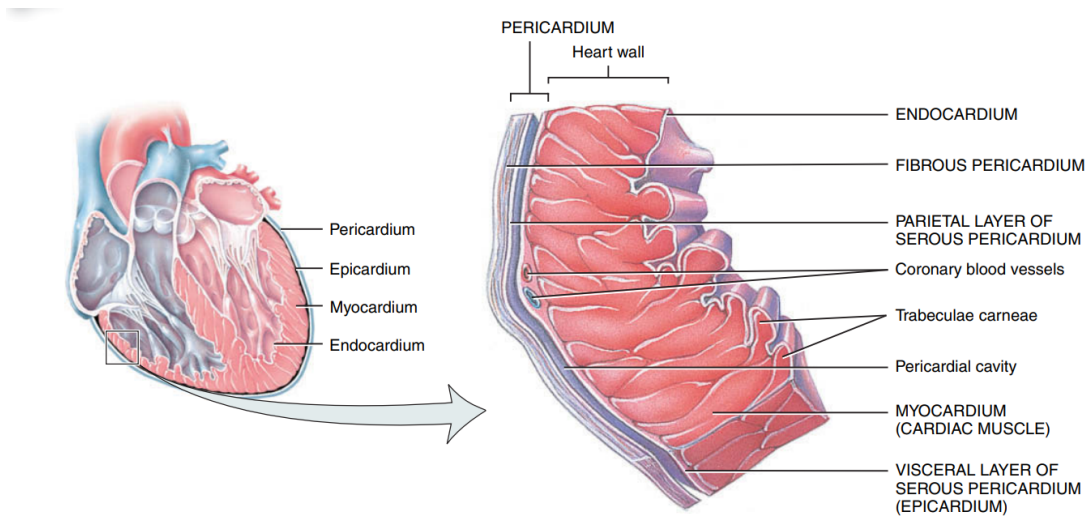


Figure. 2.2. The heart layers. Labeled illustration of the pericardium, epicardium, myocardium and endocardium of the heart. (Retrieved from [17])

The heart is a pump and to properly understand its behavior, and relevance within the body, it will be necessary to illustrate its main components and structure.

2.1.1. Anatomy of the heart

The heart is divided into two main parts, the right side, that propels blood to the lungs (pulmonary circulation), and the left one, that interacts with the peripheral organs (systemic circulation). Each side is subdivided into two chambers, the atrium and the ventricle. Additionally, the heart is connected to the circulatory system by means of veins and arteries through which blood flows in and out respectively. More specifically, atria receive blood from veins, the pulmonary veins in the case of the Left Atrium (LA) and the vena cava in the case of the Right Atrium (RA). On the other hand ventricles eject blood out through the arteries that leave the heart, more particularly, the pulmonary trunk exits the Right Ventricle (RV), and the aorta leaves the Left Ventricle (LV). Atrium and ventricle are connected by a valve, the Atrio-Ventricular (A-V) valve. More specifically, the tricuspid valve links the RA to the RV; and the mitral valve joins the LA together with the LV. The semilunar valves connect the right and left ventricles to the corresponding arteries.

Figure 2.3 illustrates the anatomy of the heart chambers just mentioned, together with

the motion of blood within the cavities.

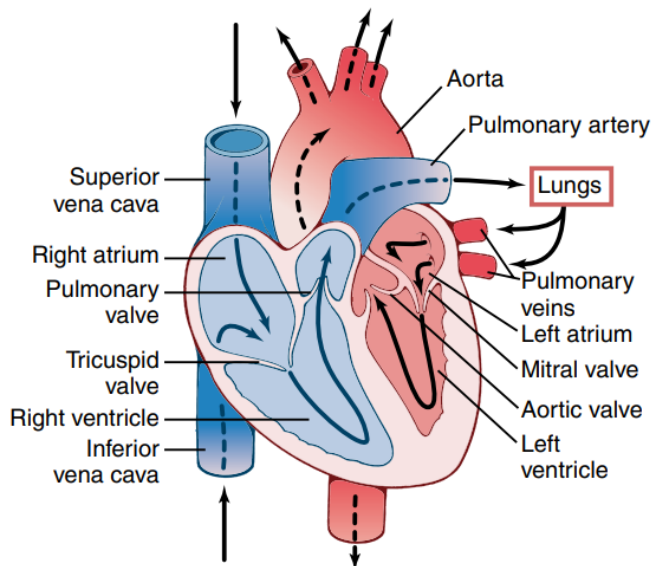


Figure. 2.3. The heart anatomy. Sectional plane of a heart, sketching the chambers and flow of blood. Blue areas represent the pulmonary circulation and the trajectory of deoxygenated blood (RA-RV). Red areas illustrate the systemic circulation and the trajectory of oxygenated blood (LA-LV). (Retrieved from [13])

2.1.2. Physiology of the heart

The cardiac cycle is the process involving a series of pressure changes taking place within the heart and allowing the blood to move through the heart chambers to the rest of the circulatory system [18]. This synchronized propulsion of blood will be intrinsically related to the electro-chemical changes happening within the myocardium, that lead to the contraction of the cardiac fibers.

The Conduction System

The network of cells characterized by generating and propagating cardiac impulses, is referred to as the Cardiac Conduction system [19]. Figure 2.4 represents this arrangement of cell units (cardiomyocytes), that fuse to one another by membranes (intercalated discs) composing the muscle fibers. The cardiac impulse propagates along the tissue thanks to communicating junctions (gap junctions), that consist in channels between adjacent cardiac cells and mediate the cell-to-cell exchange of ions and small metabolites [20].

The contraction of cardiac cells and tissue, is triggered by the depolarization of the plasma membrane. Myocardial cells allow Action Potentials to spread through the gap junctions, arriving to each and every cell and inducing their contraction [21]. Conduction begins in the Sinoatrial (SA) node, located at the junction of the superior vena cava and

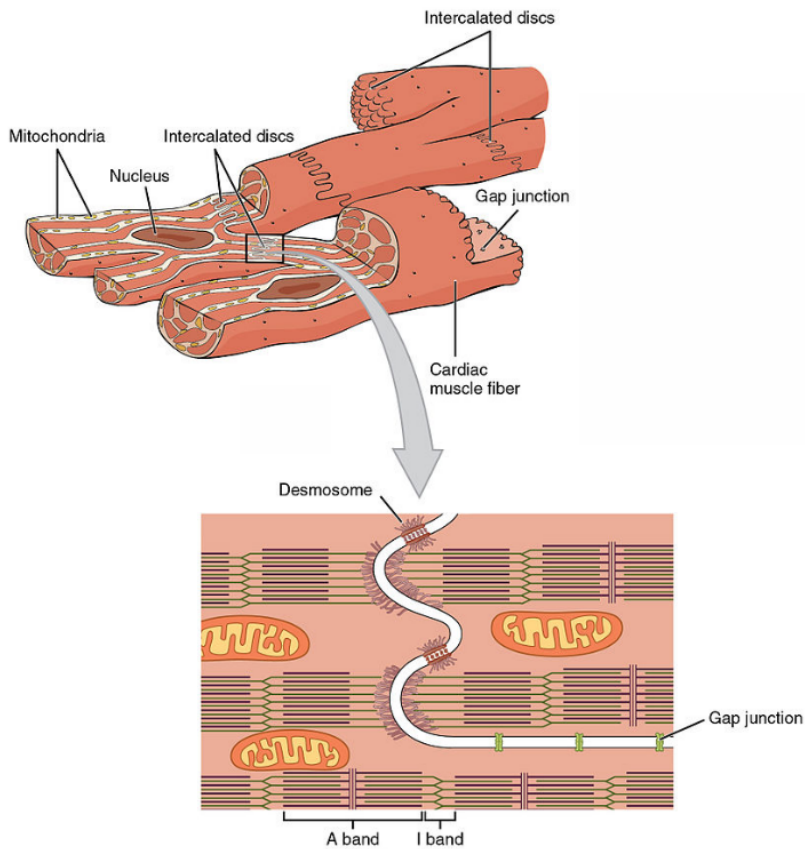


Figure. 2.4. The cardiac muscle. **A** Illustration of a muscle fiber composed of two myocardial cells with their corresponding nuclei and linking intercalated discs. **B** Detailed description of the structure of a cardiac fiber and the gap junctions through which the AP is conducted (Retrieved from online source).

the RA. It is the heart's natural pacemaker that normally initiates and synchronizes the electrical excitation of the fibers.

The Action Potential (AP) can be defined as the sequence of excitations and recoveries within cardiac cells, and inscribed by the movement of Na^+ , K^+ and Ca^{2+} , through different voltage or ligand gated ion channels [22]. This results from the opening of two types of channels: fast sodium channels and slow sodium channels (or calcium sodium channels).

At rest, a cardiac cell membrane is permeable to K^+ , since for normal concentrations of the ion, the equilibrium potential of K^+ is close to that of the myocyte (which typically ranges between -80 and -90 mV). When there is a perturbation of the membrane potential (due to an AP), voltage gated channels open and admit Na^+ . This influx of Na^+ into the cell results in a rapid depolarization of the membrane potential towards the equilibrium potential of Na^+ (+70 mV). Almost immediately, the Na^+ influx shuts off, linked to the inactivation of the Na^+ channels. When this happens, voltage-gated Ca^{2+} and K^+ chan-

nels open, leading to an influx of Ca^{2+} and an outflow of K^+ . When the outflow of K^+ dominates, the repolarization of the membrane potential is gained, making the cardiac cell go back to its resting potential [23].

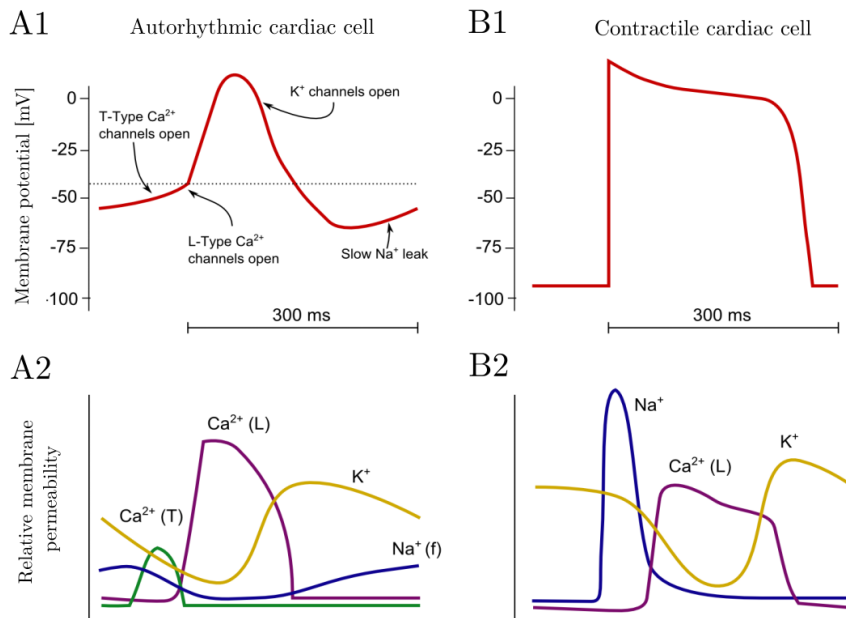


Figure. 2.5. Myocardium potential. **A1** Graphical description of the membrane's potential of a pacemaker cell. **A2** Permeability of autorhythmic membrane for Ca^{2+} , K^+ and Na^+ ions. **B1** Graphical description of the membrane potential of a contractile cardiac cell. **B2** Permeability for Ca^{2+} , K^+ and Na^+ ions of contractile's membrane (Retrieved from online source).

All cardiac cells have the ability to conduct the cardiac impulse, nonetheless, only a reduced population of those myocytes (autorhythmic cells) has the pacemaker capacity to generate the AP [24]. The main difference between a contractile and an autorhythmic cardiac cell relies on the AP plot (see Figure 2.5). In an autorhythmic cell (pacemaker), the resting potential is not steady, instead, it is characterized by a slow depolarization, up to a threshold point, where an AP event takes place. Once the AP is over, the cell membrane repolarizes and the gradual depolarization takes place over and over. Conversely, contractile cardiac fibers have a steady membrane resting potential, this plateau region or steady depolarization is maintained until the beginning of the next cardiac cycle [25].

Once explained the chemistry behind an AP event, it is relevant to go over the conduction process that takes place within the heart, and whose structure is illustrated in figure 2.7.

A cardiac pulse begins in the SA node. Each AP propagates through both atria via gap junctions, and causes both cavities to contract simultaneously. Conducted along the internodal pathways, the AP reaches the A-V node, which is located in the inter-atrial septum. At this stage, the cardiac impulse will slow down for the atria to finish contracting and emptying all blood into the ventricles. Once the blood has been completely emptied,

the AP continues into the AV bundle, propagating and entering both the right and left bundle branches, which extend through the interventricular septum and towards the heart's apex. The Purkinje fibers will then conduct the AP from the apex upwards, propagating to the remaining parts of the ventricular myocardium. As a result, the ventricles will contract, pushing the blood through the semilunar valves and out of the chambers.

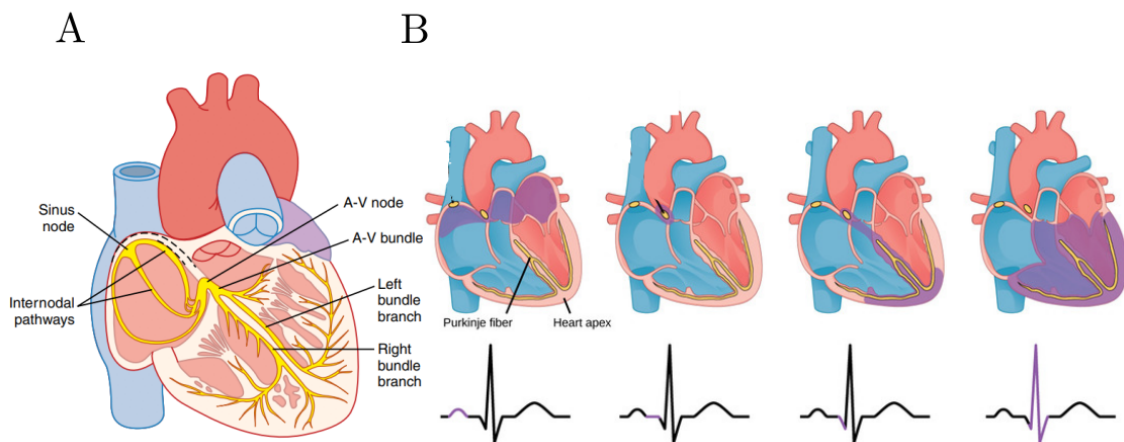


Figure 2.6. The heart conduction system. **A** Illustration of the major elements involved in the conduction of the AP through the heart. **B** Stages of the cardiac impulse transmission, an Electrocardiogram (ECG) signal is plotted below, indicating the relationship between the contraction of the corresponding atria and ventricles and the activation stage of the heart. (Created from figures retrieved from [13])

Cardiac Cycle

Linked to the arrangement of the conduction system, there is a delay of approximately 0.1 seconds in between the contraction of the atria and the ventricles. For this reason, the atria will be the primer pump, contracting and sending the blood into the ventricles; which will in turn provide the major force for pumping blood out to the cardiovascular system.

To properly explain the cardiac system we must decompose it into the diastolic phase, or period of relaxation; and the systolic phase, or period of contraction [24], [26].

The diastolic stage of the cardiac cycle involves the process of blood flowing into the atria from the great veins. Once the A-V valves are open, it enters the ventricles. Normally, 80% of the blood flows passively into the ventricles, the remaining 20% requiring the atria to contract. Once the atrium has pushed all blood away, the A-V valve closes and the semilunar valve automatically opens. Then, the systolic part of the cardiac cycle begins, involving the contraction of the ventricle and the ejection of the blood out of the chamber through the arteries. An illustrative description of diastole and systole can be appreciated in figure 2.7.

Note that during ventricular systole, A-V valves are closed and so large volumes of blood will accumulate in the atria. Once the systole is over and the ventricular blood pressure falls again, the increased pressure of blood in the atria pushes the AV valve open again, emptying the atria once again into the ventricles and therefore repeating the whole cycle all over.

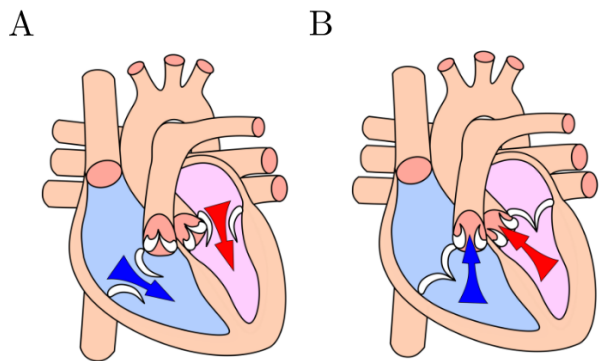


Figure. 2.7. Illustration of the cardiac cycle. **A** Diastolic stage of the cardiac cycle, involving the ejection of blood by atria into relaxed ventricles **B** Systolic stage of the cardiac cycle, contracted ventricles ejecting blood out of the heart through the aorta and pulmonary arteries. (Retrieved from [21])

Notice as well the major role of the heart valves within the cardiac cycle. They are in fact cornerstones in the prevention of blood back-flowing from the ventricles to the atria (in the case of A-V valves), and from the aorta and pulmonary arteries back into the ventricles (semilunar valves) [27]. The simple mechanism behind their intricate performance is based on closing passively when a backward pressure gradient tries to push blood back. Similarly, when a forward pressure gradient pushes blood in a forward direction, they open passively as well [28].

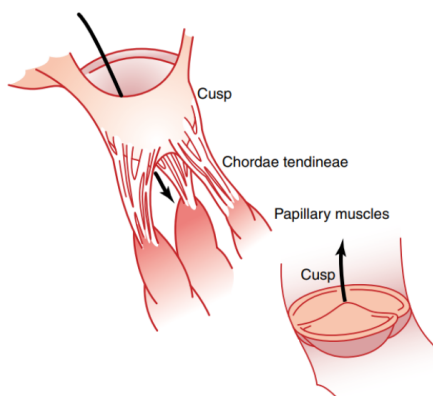


Figure. 2.8. Illustration of a heart valve. **Top image.** Heart valve pushed open and allowing blood to flow in the forward direction. **Bottom image.** Closed heart valve impeding the backflow of blood. (Retrieved from [13])

Heart activity being measured

To measure the activity of the heart cells, an electrocardiogram (ECG) is required. It is the major instrument for the diagnostic of cardiac electrophysiology [29], based on the potential difference between an arrangement of measuring electrodes (lead) the simplest one involving a pair of electrodes.

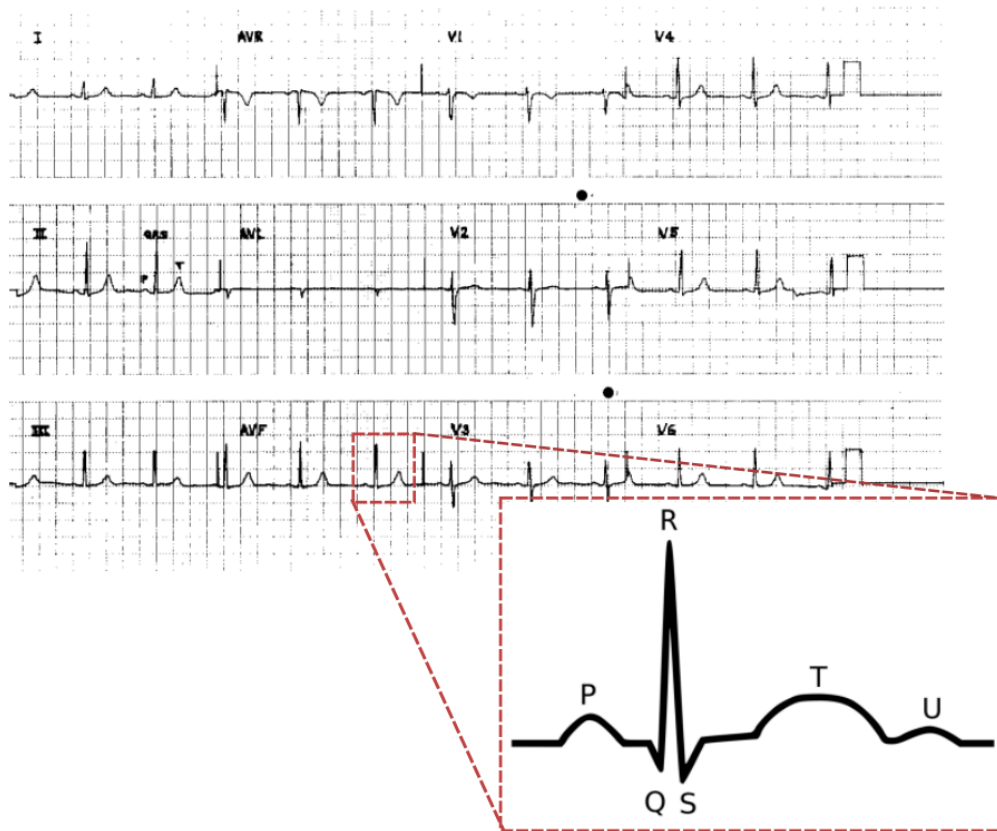
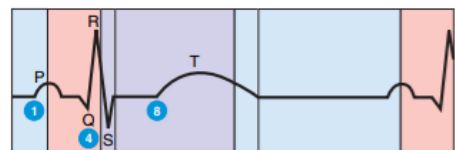


Figure. 2.9. The ECG. Description of a conventional 12 leads ECG composed of Lead I, II, III, Augmented leads (aVR, aVL and aVF), and the 6 pre-cordial leads (V1-6). An augmented morphological definition of a cardiac pulse illustrates the P wave, QRS complex and T wave. (Retrieved from [29])

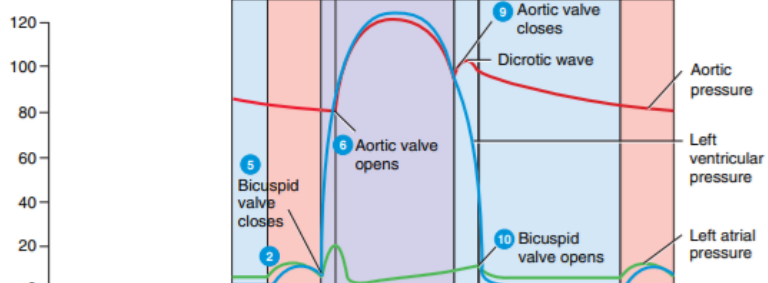
During a cardiac cycle, four deflections are visible from each lead of the ECG (see figure 2.9). The first wave, P wave, indicates the electrical activation of the atria (atria depolarization), which contract propelling blood into the ventricles (diastole). The next deflection in the lead is the QRS complex, resulting from the depolarization of the ventricles, which contract ejecting the blood out of the heart (systole). The ST segment corresponds to the time the ventricles remain contracted. It is followed by the T wave, resulted from the recovery period of the ventricles (repolarization). Normally T wave would represent the end of the cardiac cycle. U wave, rarely seen, is related to the repolarization of the papillary muscles of the heart, attached to its walls and responsible for the valvular function [29]. Figure 2.10 summarizes the main events taking place in a heartbeat, from an electrical, chemical and anatomical point of view [18].

A

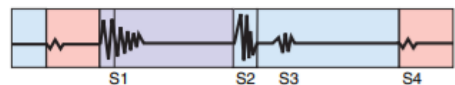


0.1 sec	0.3 sec	0.4 sec
Atrial systole	Ventricular systole	Relaxation period

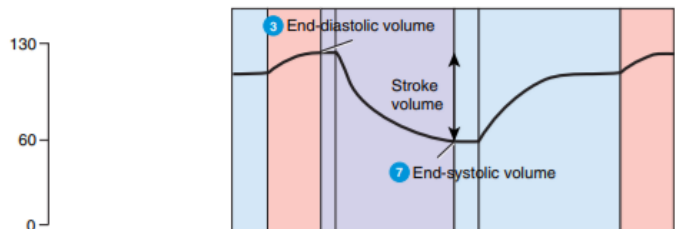
B



C



D



E

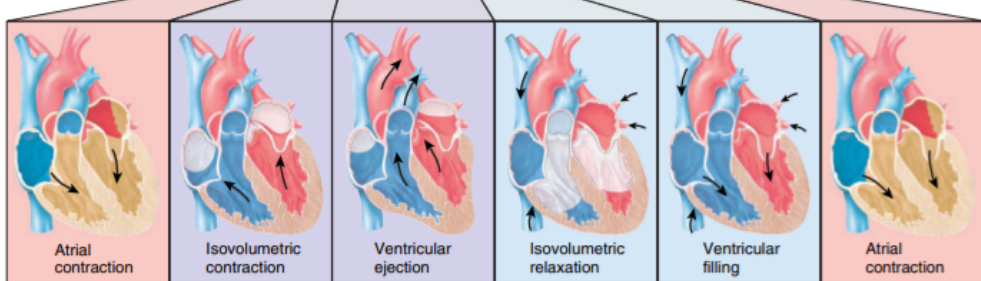


Figure 2.10. Events associated with one heartbeat. A ECG B Representation of the blood pressure changes in mmHg within the left atrium (in green), left ventricle (in blue), and in the aorta (in red). C Heart sounds D Volume changes of blood (in mL) within the left ventricle. E Illustration of the stages of the cardiac cycle. (Retrieved from [18])

2.2. Arrhythmogenesis

Heart failure is one of the major causes of morbidity and mortality in western countries, resulting in one of the greatest challenges to modern medicine and health economics [30]. Some of the most serious distressing types of heart malfunction occur because of

an abnormal rhythm [13]. The heart normally beats at sinus rhythm, where the beat is spontaneously generated by the SA node, producing the propagating electric wave that spreads through the chambers, as it has already been mentioned [31]. However, when there is a defect in the cardiac conduction system, an abnormal rythm is observed, also described pathologically as an arrhythmia [17]. In an arrhythmic heart, the coordination in the contraction of atria and ventricles is lost, with an abnormal initiation of the cardiac excitation, an abnormal propagation of the excitation wave, or a combination of both. Several cardiac diseases related to arrhythmias can be observed in figure 2.11.

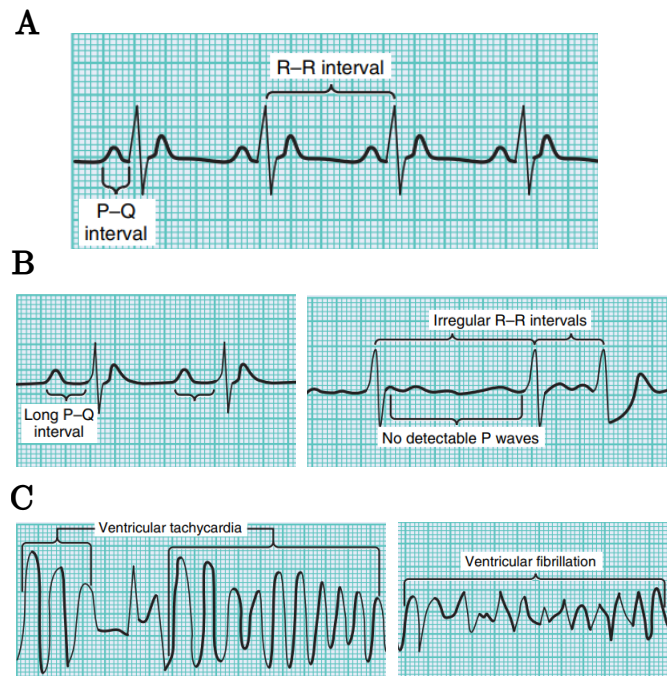


Figure. 2.11. Examples of arrhythmia-induced cardiomyopathies. **A** Normal electrocardiogram. **B** Example of atrial arrhythmias. Left, an ECG of a heart suffering from first degree A-V block. Right, ECG of an atrial fibrillation. **C** Ventricular arrhythmias. Left figure represents the ECG from a case of ventricular tachycardia. On the right, representation of a ventricular fibrillation ECG. (Retrieved form [17])

One can find various types of arrhythmogenic conditions depending on the speed, rhythm and origin of the pathology. Starting with bradycardia which is described as a slow heart rate [32] that when linked to some kind of heart condition, can be sign of conductive tissue disease [33], [34]. Tachycardia on the other hand refers to a rapid heart rate, which produces dilated cardiomyopathies involving all cardiac chambers. When there is rapid pacing, there is a disruption of both the extracellular matrix architecture and the myocyte basement membrane [35]. This cardiac substrate disruption compromises myocyte alignment, force coupling and transmission of the pulse, factors linked to the thinning of the chamber walls and the loss in contractile function.

The last kind of arrhythmogenic origin is the uncoordinated heart beat, which is a precursor to sudden heart death or fibrillation [36]. It is described as a turbulent cardiac

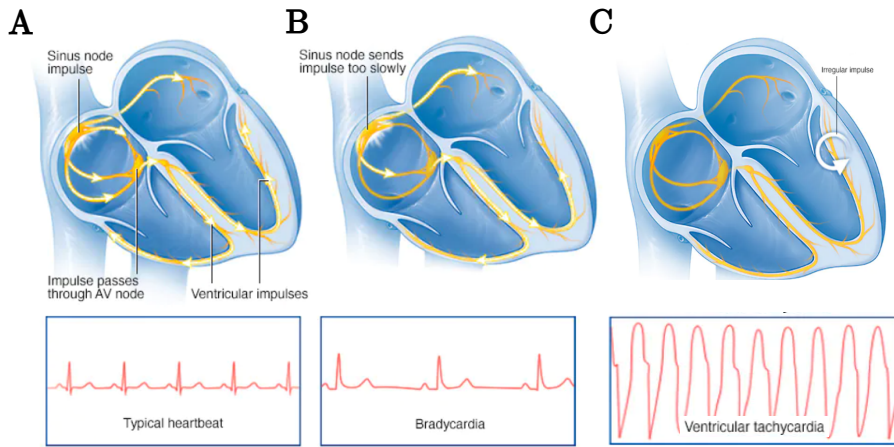


Figure 2.12. Bradycardia and Tachycardia. A Typical heart rythm with illustration of the wavefront propagation and the electrocardiogram. B Illustration of a bradycardia within the heart and its corresponding ECG. C Representation of the wavefront propagation in a heart suffering from a ventricular tachycardia with its corresponding ECG (Retrieved form online source)

electrical activity with a severe disturbance in the propagation of electrical waves through the heart [37], which culminates in an inability of the myocardium to contract.

2.3. Cardiac Fibrosis

Almost all kinds of heart diseases are associated with the process of myocardial remodelling, which is triggered by tissue fibrosis [38]. At a site of injury, fibroblasts will normally place Extracellular Matrix (ECM) proteins to replace parenchymal tissue [39]; collagen and ECM remodelling are regulated by the combined action of different inhibitors, that control the amount of collagen being distributed to the damaged tissue.

Tissue fibrosis consists in the excessive accumulation of the ECM components, which take place when the amount of new collagen synthesized outpaces its degradation, and results in an excessive aggregation within the local damaged area [40]. In the heart, fibrosis leads to the increased matrix stiffness which culminates in abnormalities in the cardiac function [41]. The anomalous conduction of the activation wavefront, including an increased heterogeneity, the generation of conduction blocks and/or reentries [42], are some of the major defects triggered by this cardiac fibrosis.

Figure 2.13 illustrates a case of myocardial fibrosis. Note that the increased collagen deposition observed in the figure, will result in myocyte electrical decoupling, which will affect both conduction and the cardiac impulse formation, leading to the just mentioned conduction slowing and an heterogeneous propagation.

Different mechanisms of cardiac fibrosis can favor the maintenance of cardiac arrhythmias [41], depending on factors such as the amount and the texture of the fibrosis.

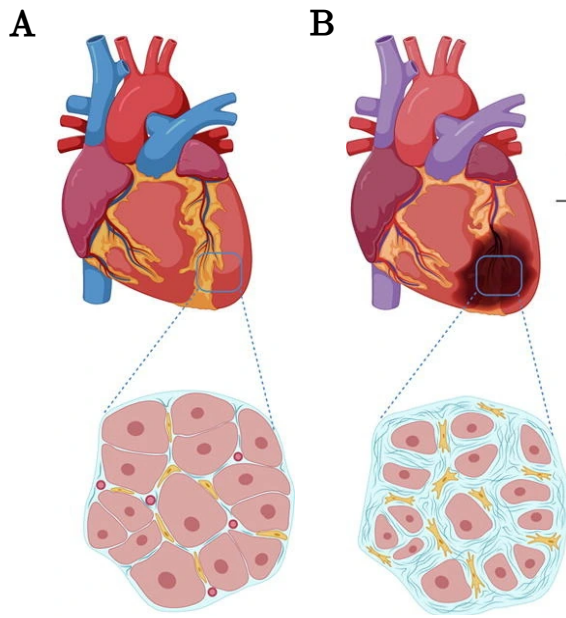


Figure. 2.13. Cardiac Fibrosis. Illustration of the cardiac tissue suffering from fibrosis. **A** Normal cardiac tissue. **B** Cardiac fibrosis microenvironment. (Retrieved from online source)

Compact fibrosis for instance, which contains substrate areas deprived of myocytes, favors arrhythmias by anchoring the re-entrant waves. A re-entrant wave occurs when a propagating impulse does not die out after normal activation of the heart, but it rather persists to re-excite the heart after expiration of the refractory period [43]. It is still unclear the details in the dependency of re-entries and the changes of the heart linked to fibrosis [44], it is however a usual indication for ablation.

Catheter or radio-frequency ablation (see Figure 2.14) commonly takes place to treat these types of fibrotic tissues. The procedure involves guiding a tube into the heart, to damage the regions responsible for an abnormal heart rythm. More specifically, it consists in burning the area, by means of different types of local energy delivery hot or cold. As a result, a scar is formed, preventing or blocking undesired electric impulses or problematic re-entrant waves, and therefore preventing abnormal rhythms [41].

2.3.1. Tissue characterization

In order to properly guide the ablation catheter to the problematic areas, it is relevant to first characterize the tissue. Catheter mapping is a diagnostic technique commonly used to identify the location and source of abnormal electrical activity in the heart [45]. Compared to other more conventional diagnostic tests, catheter mapping offers multiple advantages. To begin with, it provides a more accurate description of the location and the source of the arrhythmia, which can help provide a more personalized treatment [46].

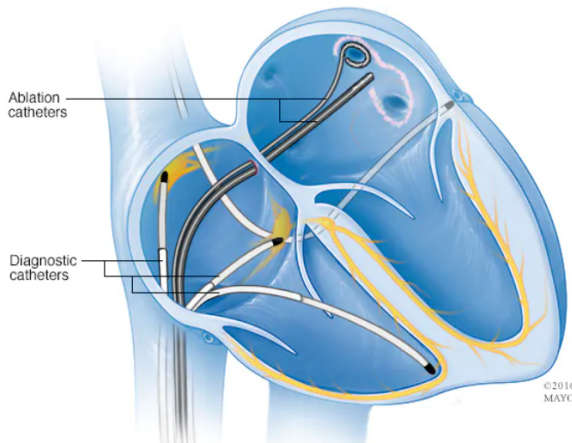


Figure. 2.14. Catheter ablation. Illustration representing ablation catheters applied near the pulmonary veins in a procedure called pulmonary vein isolation. (Retrieved from online source)

Being a minimally invasive technique is another asset of this procedure, as it involves inserting a catheter into the heart through a small incision in the groin or neck. Moreover, catheter mapping is often used in conjunction with an ablation catheter, thus guiding in the ablation procedure [47].

High Density electrode catheters are commonly used in this characterization, identifying areas of low voltage, fibrosis, re-entry, etc [48]. In fact, the chaotic propagation of the depolarization wavefront during Atrial Fibrillation (AF) for instance, can be studied by means of multiple electrophysiological parameters [49].

To present some of the most commonly studied biomarkers for electrophysiologic characterization, it will be relevant to introduce the concept of the EGM. An EGM is defined as the potential difference between a pair of recording electrodes during a depolarization event [50]. There are several types of EGMs, a unipolar recording (Unipolar Electrogram (uEGM)) consists in the potential difference between an exploring electrode (within the cardiac tissue) and a reference electrode (at a hypothetically infinite distance), representing the depolarization wave that approaches and moves away from the recording electrode [51]. In a homogeneous tissue, the morphology of a uEGM can be observed in figure 2.15.

The bipolar recording (bEGM) refers to the potential difference between two minimally distanced recording electrodes, which can be also understood as the subtraction of two unipolar signals. Figure 2.16 illustrates the disposition of recording electrodes for the case of a uEGM and a bEGM.

Both uEGMs and bEGMs are reliable biomarkers for the substrate characterization, consistent in shape and timing information [10]. Nonetheless, uEGMs are vulnerable to far-field interferences [52] and bEGMs are highly dependent on the orientation of the pair of recording electrodes with respect to the propagation wavefront. It is for this reason that

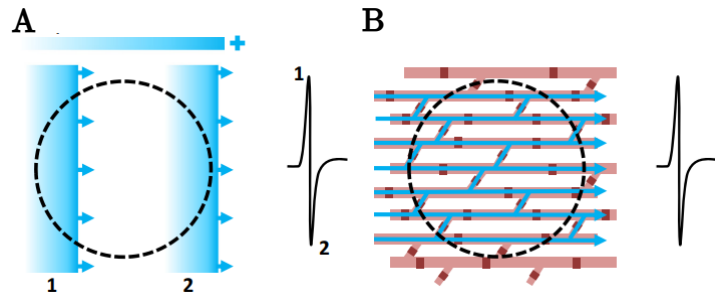


Figure. 2.15. Unipolar EGM. **A** Morphology of uEGM where the steepest point coincides with the depolarization front. **B** Homogeneous pattern of myocardial cells conducting the activation wavefront. (Retrieved from [51])

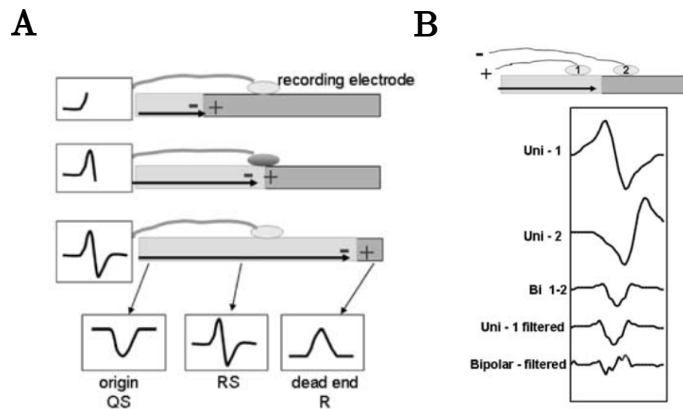


Figure. 2.16. Electrode arrangement for EGM recording. **A** Unipolar EGM. **B** Bipolar EGM (Retrieved from [50])

a novel biomarker has recently been proposed, overcoming the limitations of the previous ones [10].

The omnipole is an alternative practical method based on traditional EGMs reconstruction that attempts to design an orientation independent biomarker for a more robust identification of the fibrotic tissue. The idea is correlated to the novel type of multi-electrode catheters proposed recently, the Advisor™HD Grid Mapping Catheter (Abbott Laboratories, Illinois, US) (see Figure 2.17). This high density catheter consists in an array of 4x4 unipolar electrodes equispaced 3 mm, that is used successfully in numerous substrate exploration procedures, including for instance scars detection [53]), atrial and ventricular disorders diagnosis and treatment (i.e. AF [54], [55]).

All the above mentioned biomarkers provide relevant information to identify arrhythmogenic substrate. Low Voltage Area (LVA) correlating to fibrous tissue [56], Conduction Velocity (CV), Local Activation Time (LAT), Complex Fractionated Electrogram (CFAE) or peak-to-peak voltages, are some of the electrophysiological parameters that can be

measured to identify the heterogeneities and anisotropies resulting from the chaotic propagation of arrhythmogenic hearts, thus potential sites for catheter ablation [49].



Figure. 2.17. Illustration of Advisor™HD Grid. Mapping Catheter developed by Abbott Laboratories, Illinois, US

3. MATERIALS

This study is based on a database composed of EGM recordings coming from an experimental set of 9 rabbit hearts, isolated and perfused with the Langerdoff technique. The experiments belong to a previous study performed over a set of 10 rabbit hearts, to assess QT interval heterogeneities induced through local warming and cooling of an epicardial area of the hearts [57].

The experimental process involved placing a multiple electrode array consisting of 128 stainless steel electrodes (interelectrode distance 1 mm, diameter 0.125 mm) at the epicardium of the left ventricle at 37°C. The epicardial wall of the ventricle was stimulated with a bipolar electrode (diameter 0.125 mm, interelectrode distance 1mm) fixed at a constant position, proximal to the external lateral side of the recording electrode and connected to a GRASS S88 stimulator equiped with a stimulus isolated unit.

A total of thirty-eight recordings from 9 retrospective experiments were used for the conclusive results we derived in this dissertation. More specifically, two recordings per heart were used, stimulated at 4 and 6 Hz and three series were selected per recording. The stimuli were applied via a train of 2 ms pulses with voltage of twice the diastolic threshold.

The EGM recordings were then obtained through a cardiac electrical activity mapping system (MAPTECH; Waalre, The Netherlands). All recorded signals were amplified with a gain of 100-300, bandpass filtered (1-400 Hz) and digitised with a resolution of 12 bits. The sampling rate was 1000 Hz per channel. Figure 3.1 illustrates the disposition of the electrode array on the epicardial wall.

These experiments were performed at the Laboratory of experimental Cardiac Electrophysiology at the Department of Physiology of the Polytechnical University of Valencia, Valencia, Spain. Note that these experiments were not carried out by the author of this thesis.



Figure. 3.1. Description of the experiment. Left, arrangement of the multielectrode array. Middle, picture of the self-manufactured multielectrode. Right, experimental setting.

4. METHODS

4.1. Acquisition of the EGM signals

All the experimental unipolar signals available at the laboratory were opened and analyzed in MATLAB. A manual selection process was performed, aiming for the acquisition of those signals with the highest quality in terms of noise and amplitude. Figure 4.1 illustrates the process of how the unipolar pulse selection was performed iteratively for the 38 signals used.

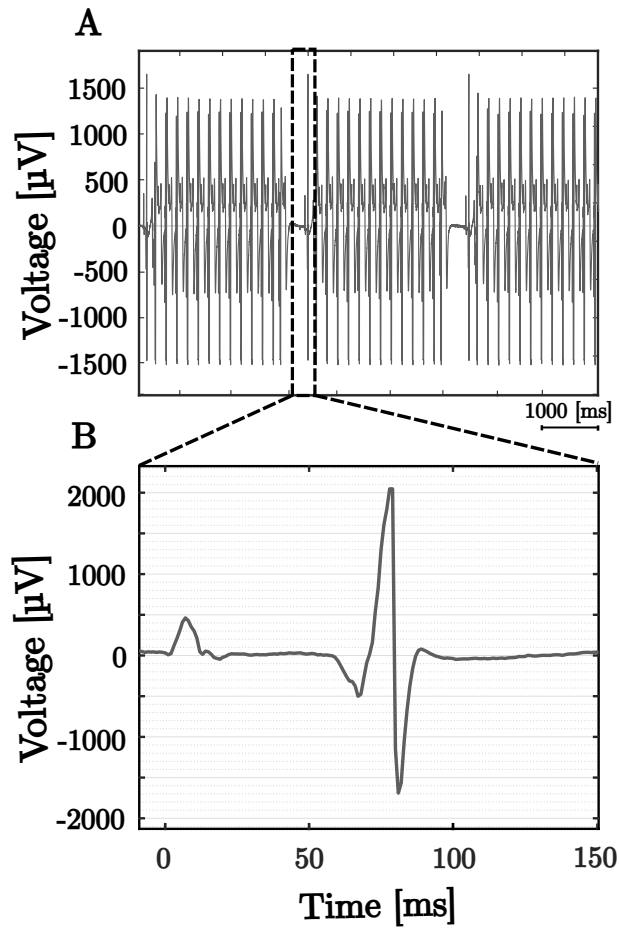


Figure. 4.1. Acquisition of a uEGM from an electrode channel. **A** 7 seconds of unipolar recordings from one channel of the multielectrode array. **B** Zoom in of a unipolar pulse.

4.2. Computation of the bEGMs

From a set of 2x2 electrodes, a clique is defined as a pair of orthogonal bEGMs. Figure 4.2 illustrates the different configurations of the electrodes of a clique to define the bipolar

axes.

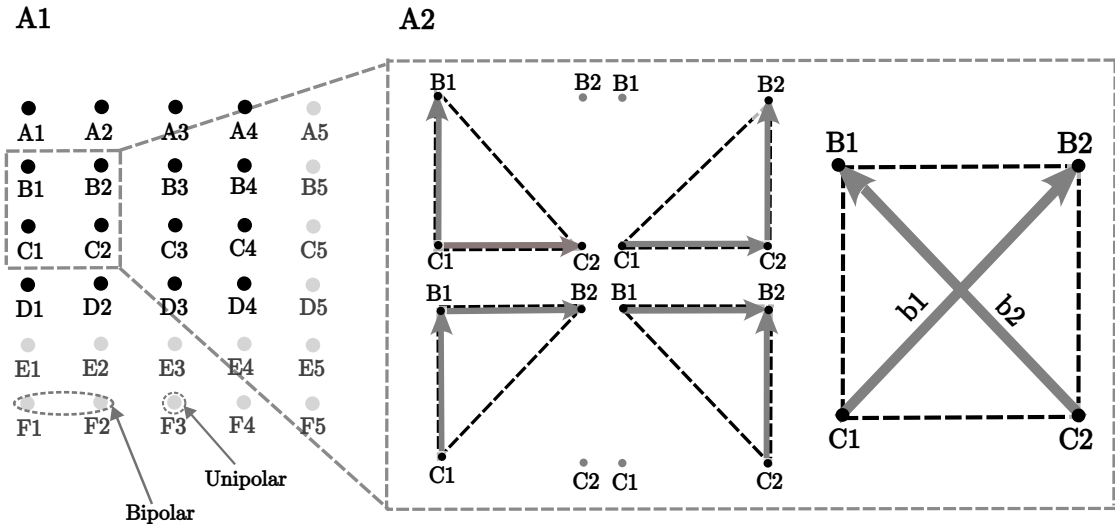


Figure 4.2. Configuration of a clique of electrodes. **A1** Catheter array with 1 mm inter-distanted electrodes, and an example of a unipolar electrode and a bipolar arrangement. **A2** Clique of electrodes zoomed in illustrating 4 triangular configurations and the cross orientation of the bipolar axes.

To describe the bipole pairs, the uEGM in a particular electrode will be referred to as $u(t)$. We will denote the triangular orientations according to the perpendicular angle location: lower left (T_1), lower right (T_2), upper left (T_3) and upper right (T_4). The cross orientation of the bipolar axes will be referred to as X. To illustrate the configuration of a cell of 2×2 electrodes inter-distanced 1 mm ($B1, B2, C1, C2$), the equations we will use for each clique configuration:

- Configuration T_1

$$b_x(t) = u_{C2}(t) - u_{C1}(t)$$

$$b_y(t) = u_{B1}(t) - u_{C1}(t)$$

- Configuration T_2

$$b_x(t) = u_{C2}(t) - u_{C1}(t)$$

$$b_y(t) = u_{B2}(t) - u_{C2}(t)$$

- Configuration T_3

$$b_x(t) = u_{B2}(t) - u_{B1}(t)$$

$$b_y(t) = u_{B1}(t) - u_{C1}(t)$$

- Configuration T₄

$$\begin{aligned} b_x(t) &= u_{B2}(t) - u_{B1}(t) \\ b_y(t) &= u_{B2}(t) - u_{C2}(t) \end{aligned}$$

- Configuration X

$$\begin{aligned} b_1(t) &= u_{B2}(t) - u_{C1}(t) \\ b_2(t) &= u_{B1}(t) - u_{C2}(t) \end{aligned}$$

Similar arrangements would be required for the case of a 2 mm inter-distanced clique (B1, B3, D1, D3), a 3 mm inter-distanced clique (B1, B4, E1, E4), and a 4 mm inter-distanced one (B1, B5, F1, F5).

In the case of the crossed oriented configuration, a clockwise rotation of $\pi/4$ of the bipolar coordinates $b_1(t)$ and $b_2(t)$ is needed as illustrated on equation 4.1. Note that the bipolar axes in the cross configuration after the angle correction, resemble the triangular arrangements augmented by a factor of $\sqrt{2}$.

$$\mathbf{b}(t) = \begin{bmatrix} \cos(\frac{\pi}{4}) & -\sin(\frac{\pi}{4}) \\ \sin(\frac{\pi}{4}) & \cos(\frac{\pi}{4}) \end{bmatrix} \cdot \begin{bmatrix} b_1(t) \\ b_2(t) \end{bmatrix} \quad (4.1)$$

If we plot the electric field, described by the orthogonally oriented bipolar axes, a loop is generated. This loop illustrates the activation pulse of the wavefront when propagating across the clique, namely at the center.

We hypothesize that the narrower the bipolar loops, the more accurate the identification of the propagation wavefront direction, as it will align with it (see figure 4.3). Similarly, wide loops pointing at random directions and lacking of any alignment are considered to be poor quality bEGMs.

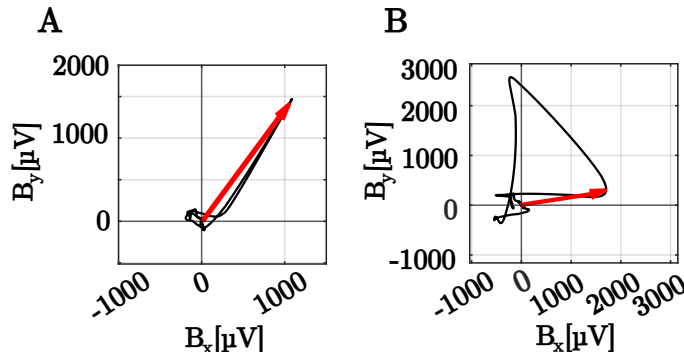


Figure 4.3. Example of the electric field loop (in black) with the activation wavefront (in red). **A**. Narrow bipolar loop, properly aligned with the propagation direction. **B**. Wide and distorted loop, incorrectly recognising the propagation direction.

4.3. Computation of the oEGM

A virtual bipole, or oEGM, is defined as a corrected bEGM such that its horizontal component is oriented parallel to the wavefront propagation. This way, when automatically computed, an omnipole would simulate a pair of electrodes from the catheter hypothetically aligning with the propagation direction, thus recording the maximum potential difference.

This is the case when the bipolar EGM has properly detected the propagation direction (by a correct alignment with this one). The oEGM is therefore reconstructed by means of a matrix rotation of the angle λ . This angle is formed by the vector of largest amplitude of the bEGM with respect to the horizontal axis

Therefore, angle λ corresponds to that wavefront propagation direction and it is computed by means of the following equation:

$$\lambda = \arctan \frac{b_y(t)}{b_x(t)} \quad (4.2)$$

The oEGM is then defined by the expression:

$$\Theta(t) = b(t) \begin{bmatrix} \cos(\beta) & -\sin(\beta) \\ \sin(\beta) & \cos(\beta) \end{bmatrix} \quad (4.3)$$

Where: $\Theta(t) = [\theta_x(t) \quad \theta_y(t)]$

The following figure illustrates these computations:

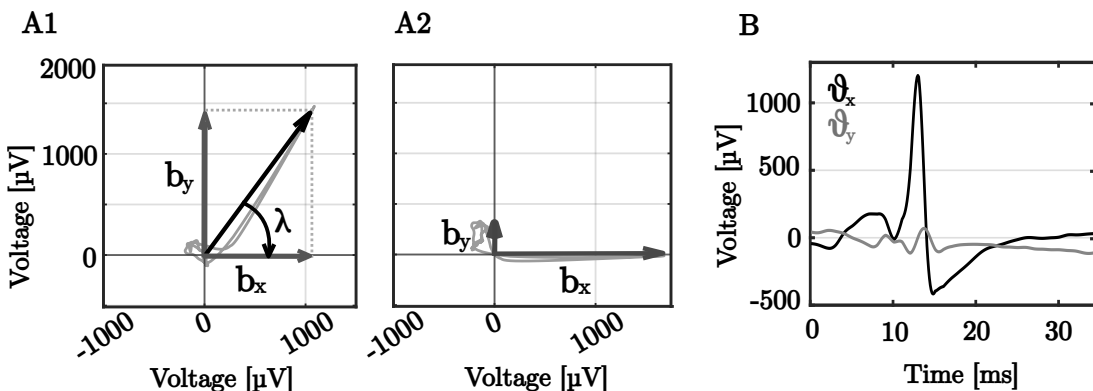


Figure 4.4. Obtention of the oEGM . **A1** Illustration of the angle λ formed by the vector of largest amplitude with the horizontal component. **A2** bEGM after rotation. **B** Resulting oEGM, where θ_x is the horizontal component of the oEGM, and θ_y the residual.

Ideally, the rotation of the bipolar matrix with the angle of wavefront propagation λ would provide a maximal amplitude to the horizontal component of the oEGM θ_x . Similarly the lowest possible amplitude is expected from the perpendicular component θ_y (residual). It is therefore hypothesized that the greater the difference in amplitude between θ_x and θ_y , the better the quality of the signal retrieved.

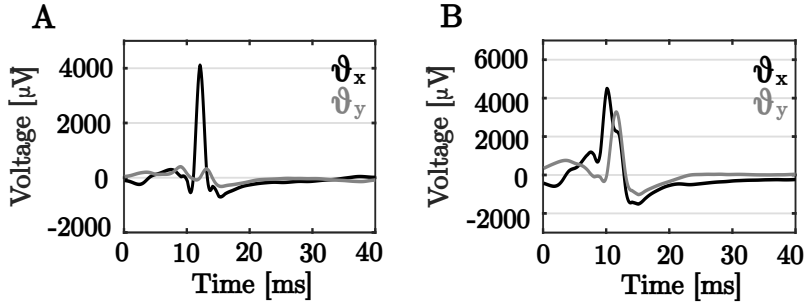


Figure. 4.5. Example of the horizontal component (in black) and vertical omni polar component (in grey). **A** High quality omni polar signal, large amplitude difference θ_x vs θ_y . **B** Low quality omni polar signal, with a poor distinction between omni polar components.

4.3.1. Unipolar reconstruction algorithm

When scrutinizing the experimental recordings and performing the uEGM pulse selection (section 4.1), some of the signals contained a region of saturation related to an inefficient amplification of the signals when they were being recorded (see figure 4.6).

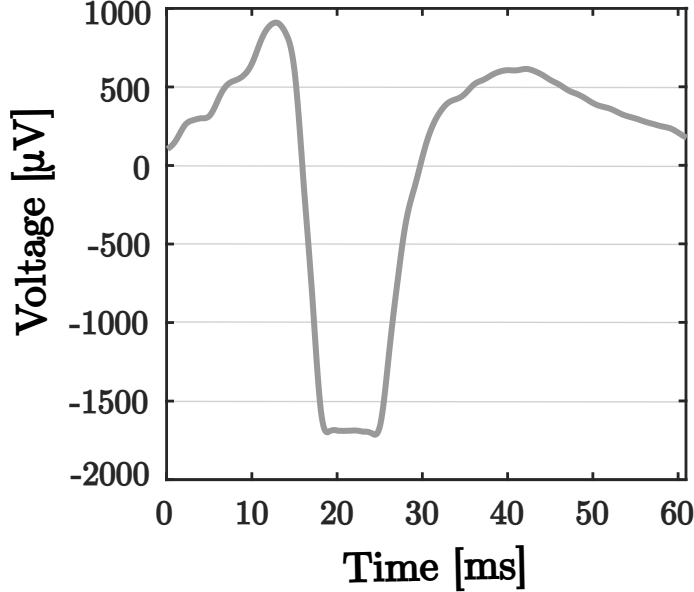


Figure. 4.6. Saturation of a unipolar signal. Example of the unipolar recordings of an electrode channel suffering from saturation at the global minima

For the purpose of retrieving the missing part of those saturated uEGMs, it was relevant to design some kind of algorithm, for the correct posterior reconstruction of the oEGM and their analysis (see figure 4.9).

The algorithm consisted in localizing the saturation region, for a posterior interpola-

tion in MATLAB.

For this purpose, we first identified the smallest voltage difference between two consecutive points of the uEGM, denoted as $\epsilon \pm \delta$, where ϵ is the smallest voltage difference, and δ the tolerance.

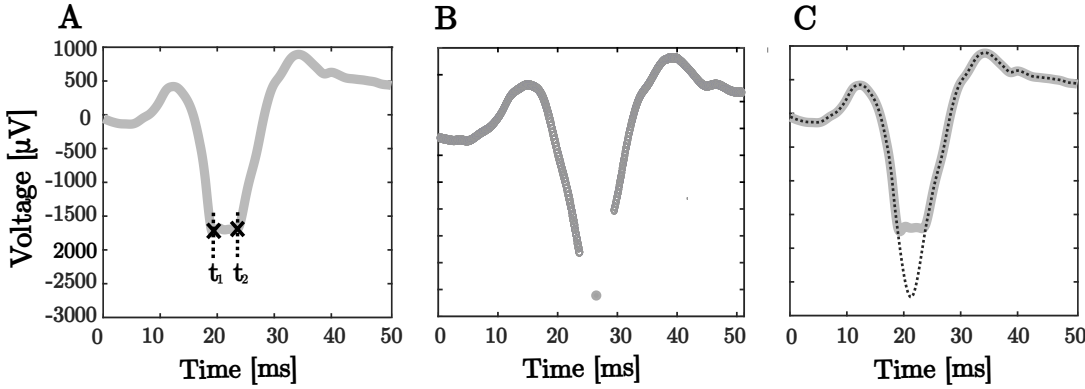


Figure 4.7. Algorithm of reconstruction. **A** Identification of the initial and final time points of the saturation region, t_1 and t_2 respectively. **B** Computation of the global minimum y_{min} . **C** uEGM reconstruction result.

If the voltage difference between two consecutive points was contained within $\epsilon \pm \delta$ for more than 4 points, it was considered that the starting point of the saturation region had been found t_1 (equation 4.4).

Whenever that condition could no longer be satisfied, namely the voltage difference between two consecutive points was no longer contained within $\epsilon \pm \delta$; then the end of the saturation region had been localized t_2 . We therefore identified a time frame restricted within that saturation region, beginning at t_1 and ending at t_2 .

$$\sum_n^{n+4} |y_n - y_{n+1}| \leq 4 \cdot (\epsilon + \delta) \quad (4.4)$$

For the morphology of the synthetic unipoles to be as close as possible to non-saturated ones, we filled the missing part of the saturated signals making use of equation 4.5. Where y_{min} is the estimated global minimum of the saturated uEGM, and y_{mid} is the voltage value at the mid-point of the saturation region.

$$\begin{aligned} \frac{|y_{min} - y_{mid}|}{|t_1 - t_2|} &= c \\ y_{min} &= y_{mid} + c \cdot |t_1 - t_2| \end{aligned} \quad (4.5)$$

The value of the constant c was estimated empirically. The procedure involved using a control unipolar signal with perfect shape. We performed a manual saturation, simulating the amplification error, then we carried out the reconstruction with 5 arbitrary values

of c , comparing the result to the original uEGM. The reconstruction that best matched the original signal was the one retrieved with $c = 2/9$. Therefore the equation for the computation of the global minima employed for all the cases of saturated uEGMs was the following:

$$y_{min} = y_{mid} + \frac{2 \cdot |t_1 - t_2|}{9} \quad (4.6)$$

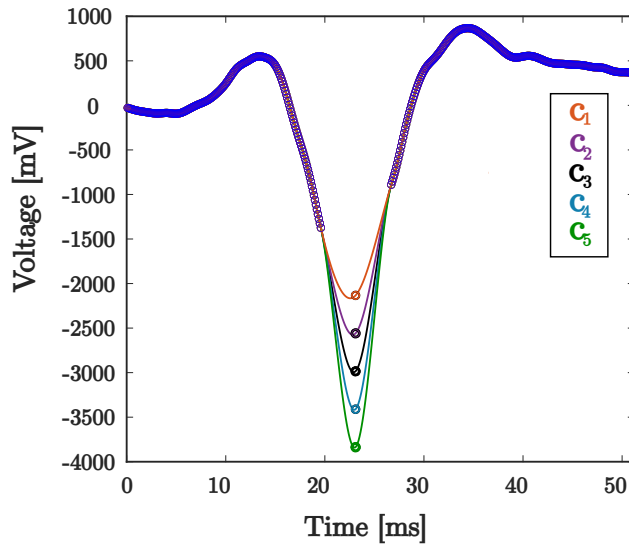


Figure. 4.8. Reconstruction of uEGM for different parameters of 'c'. Illustration of the different results of the uEGM reconstruction depending on the values of the c constant. Where $c_1 = 2/3$, $c_2 = 1/3$, $c_3 = 2/9$, $c_4 = 1/6$ and $c_5 = 2/15$

An example of the resulting oEGM from the reconstruction of a clique of saturated recordings is displayed in figure 4.9. The morphology of the oEGM retrieved with the saturated uEGMs contains a distorted region between the global maxima and minima, coincident with the saturated part of the uEGMs, that resembles the basal line, harms the quality of the results and influences the conclusions. This region of silence is smoothed, disappearing when applying the reconstruction algorithm, as observed in figure 4.9 B.

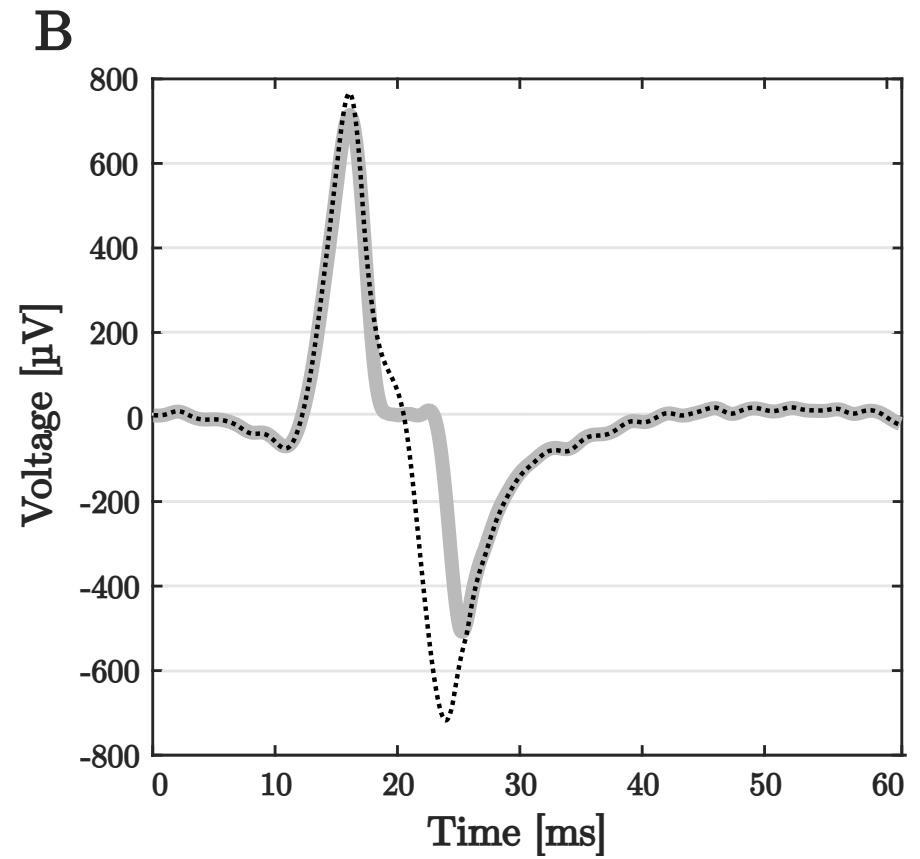
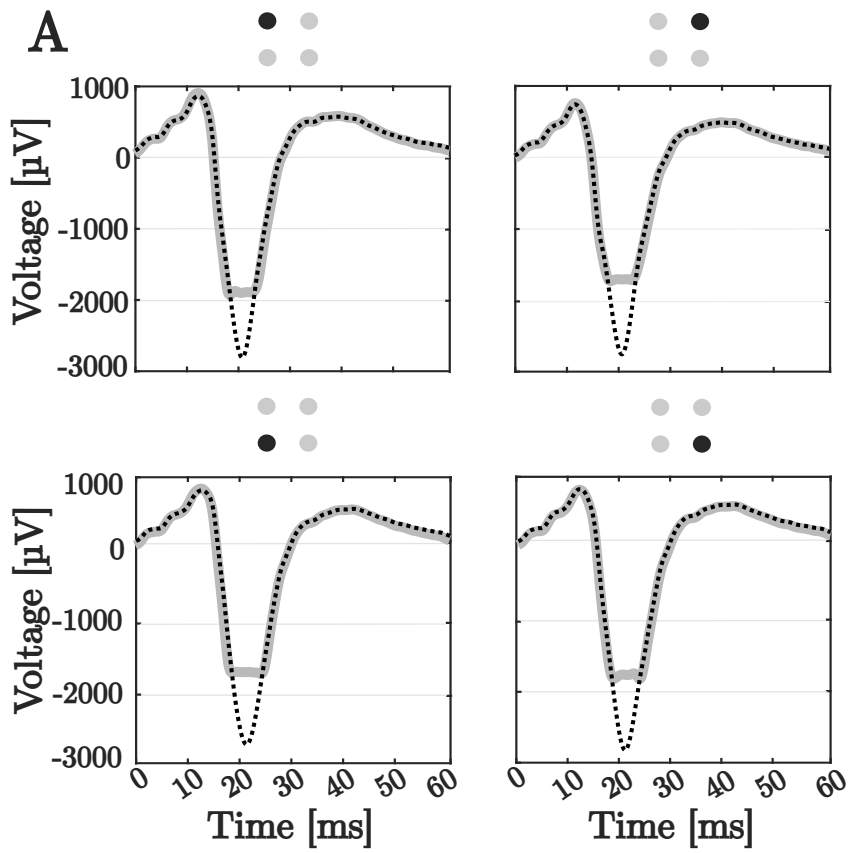


Figure 4.9. Reconstruction of a clique of saturated uEGMs. **A** Clique of saturated uEGMs in light grey, with their corresponding reconstructed unipoles overlapped in dashed black lines. **B** Resulting omnipole recovered using the saturated signals (light grey), with the reconstructed version (overlapped in dash black).

4.4. Parameters of assessment of the signals

Both bipolar and omnipolar signals were analyzed paying attention to different features. The narrowness of the bipolar loops, the magnitude of the largest omnipolar component, the distinction between omnipolar axes, the width of the pulse and the distortion of the signals, were the parameters of assessment used to determine the robustness of the resulting signals.

4.4.1. Areas of the bEGMs: NBA

The first parameter of quality evaluation is related to the area contained within the loop generated by the electric field during a depolarization event. As we hypothesized, the narrower the loop the more aligned it will be with the activation wavefront direction, thus the higher the quality of the bEGM.

We first normalized the bipolar loops for an equal clique configuration comparison to be performed, discriminating the $\sqrt{2}$ factor from the cross oriented cliques. We then estimated the areas contained within the normalized loops by means of the following equation [58] (see figure 4.10.A).

$$NBA = \iint_L \left\| \frac{\partial \mathbf{s}}{\partial \varrho} \times \frac{\partial \mathbf{s}}{\partial \xi} \right\| d\varrho d\xi \quad (4.7)$$

4.4.2. Amplitude of the oEGM: OA

The robustness of the omnipolar signals is also assessed, starting with the amplitude of the component ideally aligned with the activation wavefront, θ_x (see figure 4.10.B).

We will assume that high quality oEGMs have properly oriented θ_x component with large amplitude values.

4.4.3. Ratio of the oEGM: OR

In coherence with the previously described parameter, the ratio of omnipolar components is described by equation 4.8.

We hypothesize that the greater the distinction between omnipolar components, the greater the OR parameter, thus the more robust the signal will be (see figure 4.10.B).

$$OR = \frac{|\theta_x(t)|}{|\theta_y(t)|} \quad (4.8)$$

4.4.4. Width of oEGM pulse: OW

The Omnipolar Width (OW) is a key metric that reflects the duration of a single pulse. It is calculated as the time elapsed between the leading edge, which is the start of the pulse, and the trailing edge, which is the end of the pulse. This information is critical to understand the accuracy of the estimated oEGM (figure 4.10.C).

The reasoning behind the importance of OW is related to the concept of morphology distortion. This refers to changes in the shape of the pulse waveform as it travels through the heart's electrical system. The longer the OW, the more distorted the pulse waveform becomes, thus more delayed the activation. As a result, the accuracy of the oEGM estimation decreases.

To ensure an accurate representation of the heart's electrical activity, it is important to have a short OW. This means that the leading and trailing edges of the pulse should be close together, indicating a sharp and well-defined waveform. By keeping the OW short, it is possible to minimize the effects of morphology distortion and obtain a more accurate oEGM calculation.

4.4.5. Distortion of the oEGM: OD

The morphological distortion (MD) of $\Theta(t)$ can be caused by inter-electrode spacing sampling. When the distance between electrodes is too large, the bEGMs $b_x(t)$ and $b_y(t)$ may not be considered as obtained from points that are infinitesimally close, thus the homogeneous and flat propagation of the wavefront across the clique cannot be assumed any longer. This can result in a noticeable delay between activations, leading to the bEGMs being viewed as subtractions of delayed versions of the uEGM, instead of representing its gradient.

We will design a theoretical oEGM (at the center of the clique), to be considered as ground truth. We will then compare it to all the oEGMs retrieved with each arrangement of the bipolar axes (see figure 4.10.D).

When unipolar waveforms are obtained from infinitesimally close sites, the ground truth oEGM at the center of the clique, $\Theta(\hat{t}, \hat{x}, \hat{y})$, can be estimated by taking the negative time derivative of the previously aligned and averaged uEGMs of the clique (see equation 4.9 [10]).

The alignment is performed to disregard the activation delays between recording electrodes. The averaging has additional advantages for the OD parameter, related to the reduction in common interferences and noise of the uEGMs.

$$\hat{\Theta}(t, x, y) = -\frac{\partial}{\partial t} \hat{u}(t, x, y) \quad (4.9)$$

When considering the electrodes of the multielectrode array, we will denote $\hat{\Theta}(t, x, y)$

simply as $\hat{\Theta}(t)$.

The OD parameter is computed after a normalization of the $\hat{\Theta}(t)$, from the root mean square error (RMSE) between that omnipolar ground truth ($\hat{\Theta}(t)$), and the normalized empirical oEGM ($\Theta(t)$).

We hypothesize that the smaller the inter-electrode distance, the higher the similarity between $\hat{\Theta}(t)$ and $\Theta(t)$, thus the smaller the error. For this reason, the smaller the value of the OD parameter the more accurate the retrieved oEGMs.

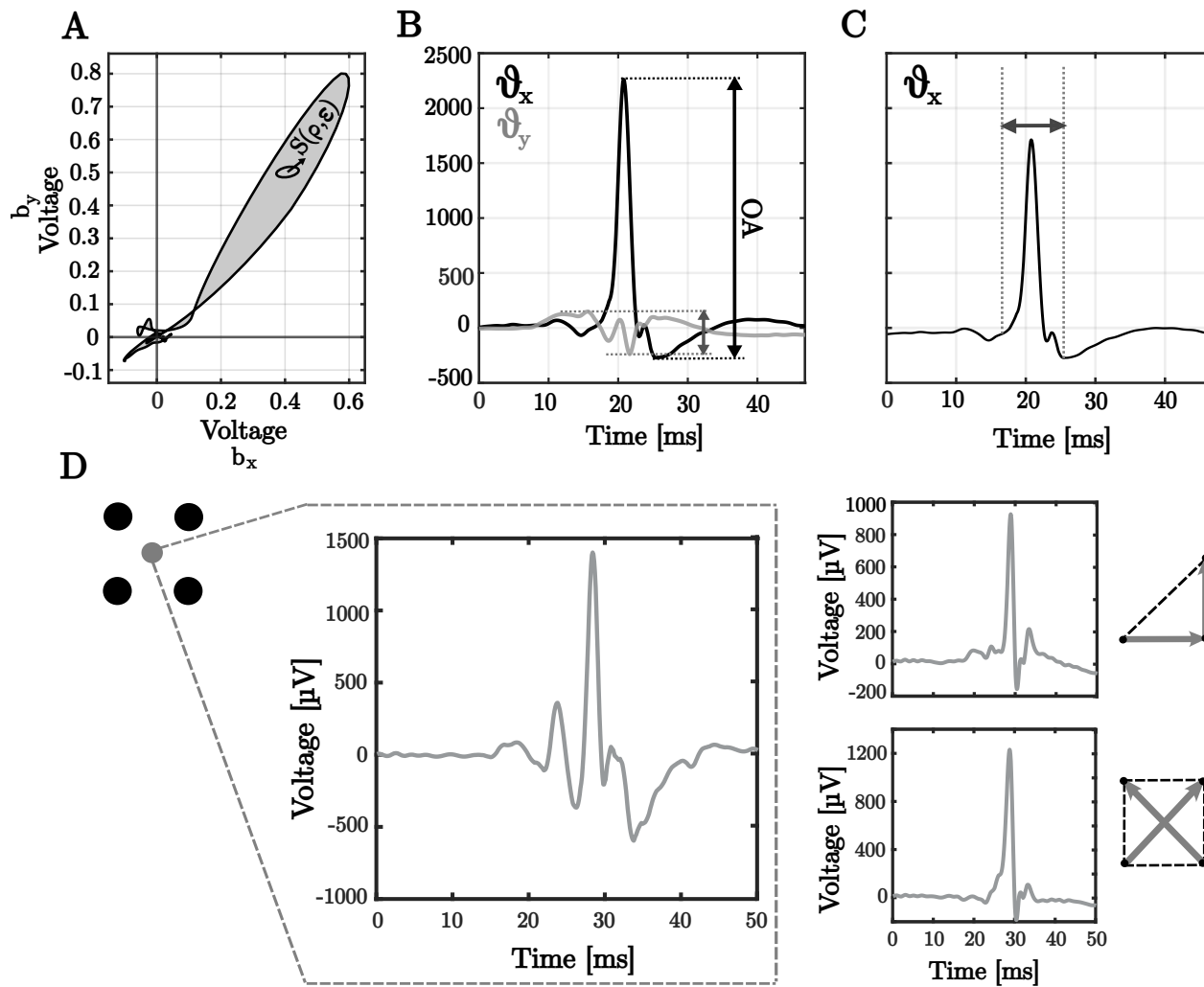


Figure 4.10. Illustration of the metrics. **A** Normalized Bipolar Areas. **B** Representation of omnipolar amplitudes to be used for the OA and OR metrics. **C** Omnipolar Width. **D** Omnipolar Distortion, ground truth omnipole (on the left), corresponding omnipoles reconstructed with T_1 and X configurations of electrodes (on the right).

4.5. Statistical Analysis

A statistical model is a formal mathematical representation of the relationship between variables in a given dataset [59]. The primary objective of constructing a statistical model is to capture the underlying patterns and relationships in the data, thereby facilitating prediction and inference. The model is represented by a set of mathematical equations where the parameters in the equations represent the relationships between variables. The prediction or inference made through a statistical model is based on retrieving response (or dependent) variables from the values of the predictor (or independent) variables.

In our study two types of statistical analyses were performed:

- Distribution of the independent variables

Evaluated by means of two statistical tests: the Kolmogorov-Smirnov test [60] and the Mann-Whitney-Wilcoxon test [61]. These tests were used to assess the shape, center, and spreading of the distribution of the independent variables, and to determine whether the data followed a normal distribution, which was not the case.

- Linear mixed-models.

A linear mixed model (LMM) is a type of statistical model used to analyze data with a multi-level or hierarchical structure [62]. It is an extension of the standard linear regression model, particularly useful when the observations are not independent and there are multiple sources of variability [63].

In a linear mixed model, both fixed-effects and random-effects terms are included in the statistical analysis. They describe the average and individual-level effects of the independent variables on the dependent variable, respectively [64]. For instance, in our study the so-called fixed-effects were the independent variables (electrodes arrangement and inter-electrode distance) as well as their interaction (configuration * distance). They were included in the linear mixed models to explain their effect over the dependent variables (metrics NBA, OA, OR, OW and OD).

The random effects in the study were the intercept for the heart origin, which was included due to the repeated measures on the same rabbit heart origins. More specifically, the inclusion of the random intercept accounts for the fact that each heart origin provides multiple observations to the data, and the random intercept allows for the modeling of the variation in the dependent variable that is due to the difference between heart origins. In other words, it accounts for the possibility that the means of the dependent variable may vary between heart origins, and that this variation is not fully explained by the fixed effects (i.e., configuration, distance, and their interaction).

In the study, two linear models are proposed, the first one includes multiple independent variables (configuration, distance, and their interaction) to predict the dependent variable (the computed metrics). In addition to the independent variables, the first model

also includes a random intercept for the sub-samples within each combination of rabbit heart origin, configuration, and distance. The inclusion of this random intercept means that the model accounts for the fact that multiple observations were taken from the same rabbit heart origins.

The second model however still includes the independent variables (configuration, distance, and their interaction) as well as a random intercept for the heart origin, but it was fit to the aggregated sub-samples instead of the raw data, meaning that multiple individual sub-samples were combined into a single, summarized sample. This process of aggregation helped to simplify the data and reduce the number of variables being considered in the model.

The statistical analysis was performed with the second model, since it was simpler and the results obtained from both tests were fairly similar. In order to check the assumptions made were correct, we performed an assessment of the Gaussianity [65] and the Homoscedasticity respectively [66].

Gaussianity refers to the assumption that the residuals, which are the differences between the observed and predicted values, are normally distributed. In other words, the residuals should follow a bell-shaped curve with a mean of zero.

The homoscedasticity on the other hand refers to the assumption that the variance of the residuals is constant across all predicted values. In other words, the residuals should be spread in a constant manner, regardless of the value of the independent variables.

To evaluate these assumptions, quantile-quantile plots and residual diagnostics were used (see Supplementary material).

A post-hoc test was then used to compare the results of the model. The purpose of this test was to determine whether the differences between the configurations and distance groups were significant, taking into account the multiple comparisons made. The post-hoc test used was the Tukey method, which is based in a correction for multiple comparisons, adjusting the p-value of each comparison to account for the number of comparisons made. In other words, the Tukey method helps to control the probability of making a type I error (probability of incorrectly assuming two groups as significantly different) when making multiple comparisons.

The results of the test were considered statistically significant if the p-value was less than 0.05. This means that there was a less than 5% chance that the observed differences between the configurations were due to chance. The statistical model and comparison tests were all performed using RStudio.

5. RESULTS

For the organized presentation of the results of this thesis, we will start by displaying the EGMs from a specific heart experiment stimulated at 4 Hz of frequency. The bEGMs and oEGMs are reconstructed using all the clique configurations defined in section 4.2 and across four inter-electrode distances.

Subsequently, a global analysis of the 38 signals is exposed, evaluating the metrics of assessment described in the previous section (NBA, OA, OR, OW and OD). For this purpose, a table containing the real magnitudes for 3 non-redundant configuration groups and at four distances is provided. A global analysis of the statistical similarity between configuration groups and inter-electrode distances is equally illustrated and quantified.

5.1. Morphological analysis of a particular signal

If we analyze a particular recording set coming from a specific heart experiment stimulated at 4 Hz; depicted in figure 5.1, are the representations of the bEGMs reconstructed using the triangular and cross configurations of the clique. The red arrows illustrate the detected direction of propagation of the wavefront across the clique.

Along 4 different inter-electrode distances, at first glance one can observe the increase in size of all the loops. For small distances ($\leq 2\text{mm}$) the bEGM loops are narrower, in general aligned with the direction of the propagation wavefront. For larger distances however ($> 2\text{mm}$), the magnitude of the loops increases.

Also noticeable is the similarity in the morphology of the bEGM loops generated by complementary configurations (T_1 vs T_4 on the one hand and T_2 vs T_3 on the other). Whereas cliques T_1 and T_4 reconstruct narrow bEGMs pointing at consistent directions, cliques T_2 vs T_3 retrieve wider loops with no precise estimation of the propagation wavefront.

Observe how the cross clique provides loops that resemble those coming from the first set (T_1 vs T_4) at all distances, with equally narrow bEGMs and apparently precise orientations, therewith the red arrows point consistently at the same direction.

From the electric loops depicting the activation of the clique, and the corresponding algebraic rotations studied in section 4.3, the oEGMs can be derived (see figure 5.2). Similarly to the previous illustration, the omnipoles are reconstructed attending to 5 different clique arrangements within 4 inter-electrode distances.

In coherence with the bEGMs, omnipolar signals increase in magnitude with a directly proportional dependency to the increase in inter-electrode distance. Also noticeable is the effect of the $\sqrt{2}$ factor in the cross arrangement, compared to the triangles. In fact, those

omnipoles computed with the cross clique are visually greater in magnitude than the rest of the oEGMs.

When focusing on the 1 mm setting, configurations T₁, T₄ and cross, provide estimates with lower amplitude of the θ_y (see figure 5.2, 1mm). Where the distance increases from 1 to 4 mm, so does the amplitude of the oEGM, which becomes wider in both axes (θ_x and θ_y).

Similarly to the amplitudes increase, the distortion of the signal and the fractionation degree are both factors that increment proportionally to the increase in electron spacing.

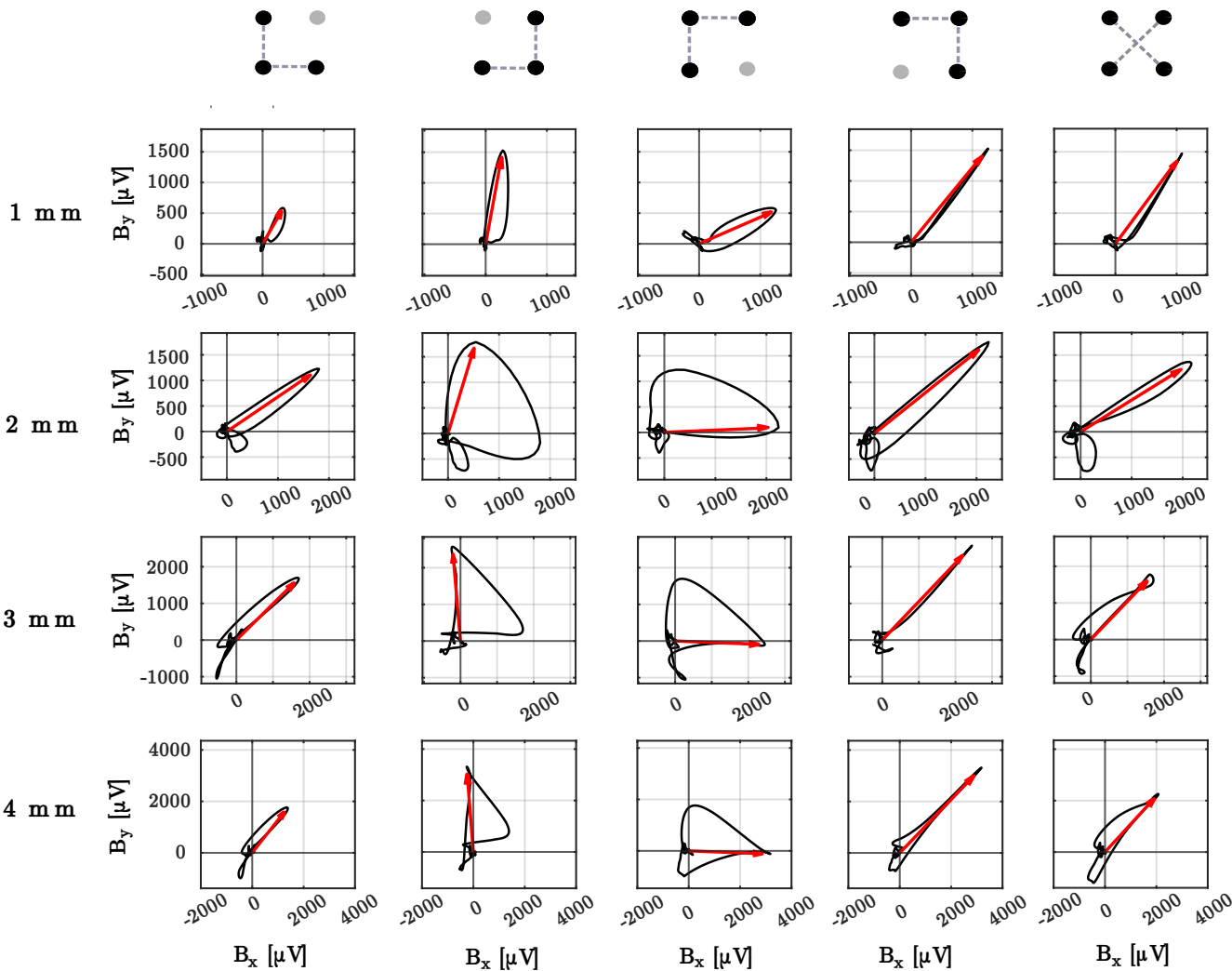


Figure 5.1. bEGMs from a signal. Represented in black are the bipolar loops retrieved from triangular and cross configurations of clique, across 4 different inter-electrode distances, with the red arrows denoting the different propagation directions detected for each case.

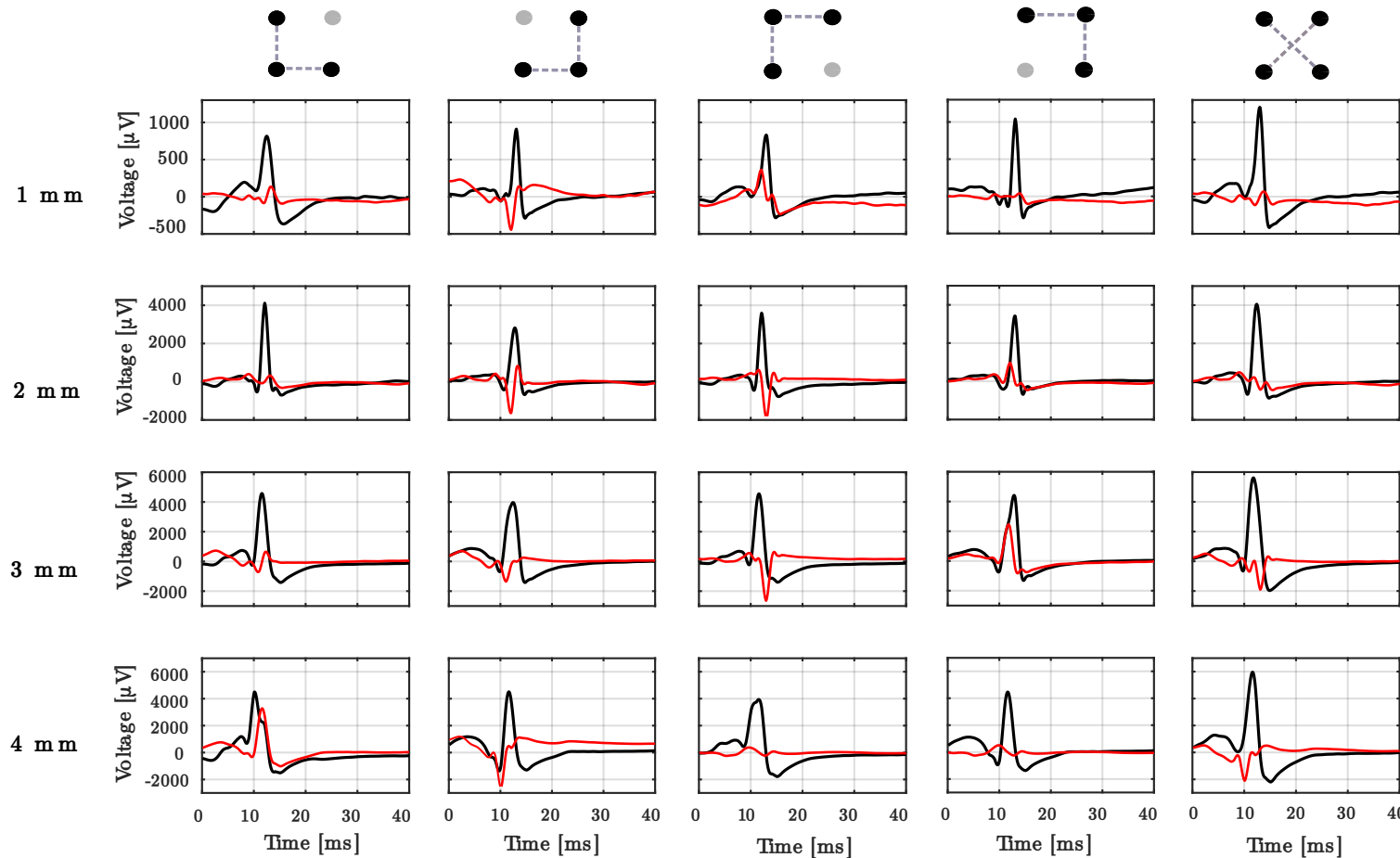


Figure 5.2. oEGMs from a particular signal. Represented in black are the horizontal components, θ_x , in red the vertical components, θ_y , across 4 different inter-electrode distances, retrieved with the different electrode configurations.

5.2. Quantitative Analysis

In addition to the experimental findings shown in figures 5.1 and 5.2, we conducted a thorough quantitative analysis of the parameters described in section 4.4 (NBA, OA, OR, OW, and OD).

Table 5.1 contains the numerical values for mean and standard deviation of the parameters of assessment for three non-redundant clique configurations within four distances. The reason why we have grouped the four triangular configurations into two groups, relies on the complementary geometry of the triangles, two-by-two, which leads to them providing similar results that have been averaged.

Coherent to the results from the bEGMs (figure 5.1), the magnitudes of larger areas correspond to those retrieved with the triangular configurations T_2 and T_3 , with an increase proportional to the distance. In fact, the loops are twice bigger than those computed with the other two triangles, and almost three times greater than the bEGMs retrieved using the cross configuration.

The ideas derived from the omnipolar plots on figure 5.2 are also coherent to the results of OA displayed on the table 5.1, and so are the OR values. Coincident to the $\sqrt{2}$ factor increase, the amplitudes from those omnipoles retrieved with the cross cliques (for the case < 2 mm) are almost that number of times greater. For larger inter-electrode distances, there is a gradual increase in amplitude where cross oriented cliques still retrieve omnipoles of bigger size.

Regarding the distinction between omnipolar axes, the OR dependency on distance can be equally observed in the table. The increase in inter-electrode distance leads to a decrease in OR magnitude.

Also noticeable is the high similarity in the performance of triangles T_1 , T_4 and the cross clique. Despite triangles provide slightly bigger OR magnitudes, for all distances (specially for < 2 mm), they retrieve similar results. Triangles T_2 , T_3 yield the smallest values for the OR magnitude at all distances.

The last two metrics of assessment, OW and OD, do not yield conclusive results when comparing clique arrangements. However, it can be noticed that again there is a dependency on inter-electrode distance, in fact omnipoles increase in amplitude but also in width, as observed in the results of OW. Additionally, the values for the metric assessing the deviation of the oEGM with respect to the ground truth ($\hat{\Theta}(t)$) (OD), also increase proportionally to the increase in distance, as the omnipoles become progressively wider.

		X	T₁ & T₄	T₂ & T₃
1 mm	NBA	0.11 ± 0.01	0.13 ± 0.01	0.27 ± 0.03
	OA [µV]	2396.21 ± 4.37	1934.35 ± 4.20	1872.90 ± 3.97
	OR	5.20 ± 0.34	5.26 ± 0.34	3.72 ± 0.38
	OW [ms]	4.32 ± 0.49	5.95 ± 0.44	4.20 ± 0.43
2 mm	OD [µV]	0.09 ± 0.01	0.11 ± 0.01	0.09 ± 0.01
	NBA	0.16 ± 0.02	0.25 ± 0.03	0.36 ± 0.03
	OA [µV]	3896.41 ± 4.91	3459.08 ± 4.92	3320.77 ± 4.89
	OR	3.49 ± 0.28	3.70 ± 0.35	2.39 ± 0.13
3 mm	OW [ms]	5.86 ± 0.49	5.46 ± 0.75	4.62 ± 0.55
	OD [µV]	0.11 ± 0.01	0.11 ± 0.01	0.11 ± 0.01
	NBA	0.23 ± 0.03	0.26 ± 0.03	0.31 ± 0.03
	OA [µV]	4461.65 ± 5.88	3944.15 ± 5.14	3791.66 ± 5.23
4 mm	OR	3.13 ± 0.25	3.28 ± 0.23	2.50 ± 0.17
	OW [ms]	6.26 ± 0.57	5.38 ± 0.49	5.20 ± 0.54
	OD [µV]	0.13 ± 0.01	0.11 ± 0.02	0.13 ± 0.01
	NBA	0.22 ± 0.02	0.28 ± 0.03	0.28 ± 0.02
	OA [µV]	4840.51 ± 5.66	4162.91 ± 5.18	4101.43 ± 5.05
	OR	2.77 ± 0.15	2.91 ± 0.20	2.75 ± 0.18
	OW [ms]	6.73 ± 0.53	6.08 ± 0.38	6.17 ± 0.37
	OD [µV]	0.13 ± 0.01	0.11 ± 0.03	0.14 ± 0.01

Table 5.1. RESULTS FOR THE DEFINED VARIABLES OF ASSESSMENT

5.2.1. Boxplots and statistical analysis

The global statistical study of the 38 cliques, reconstructed using the five methods of configuration and assessed with the five metrics of evaluation, is illustrated in the boxplots displayed below. The analysis are performed following the statistical procedure explained in section 4.5, and observable in tables 5.2 and 5.3.

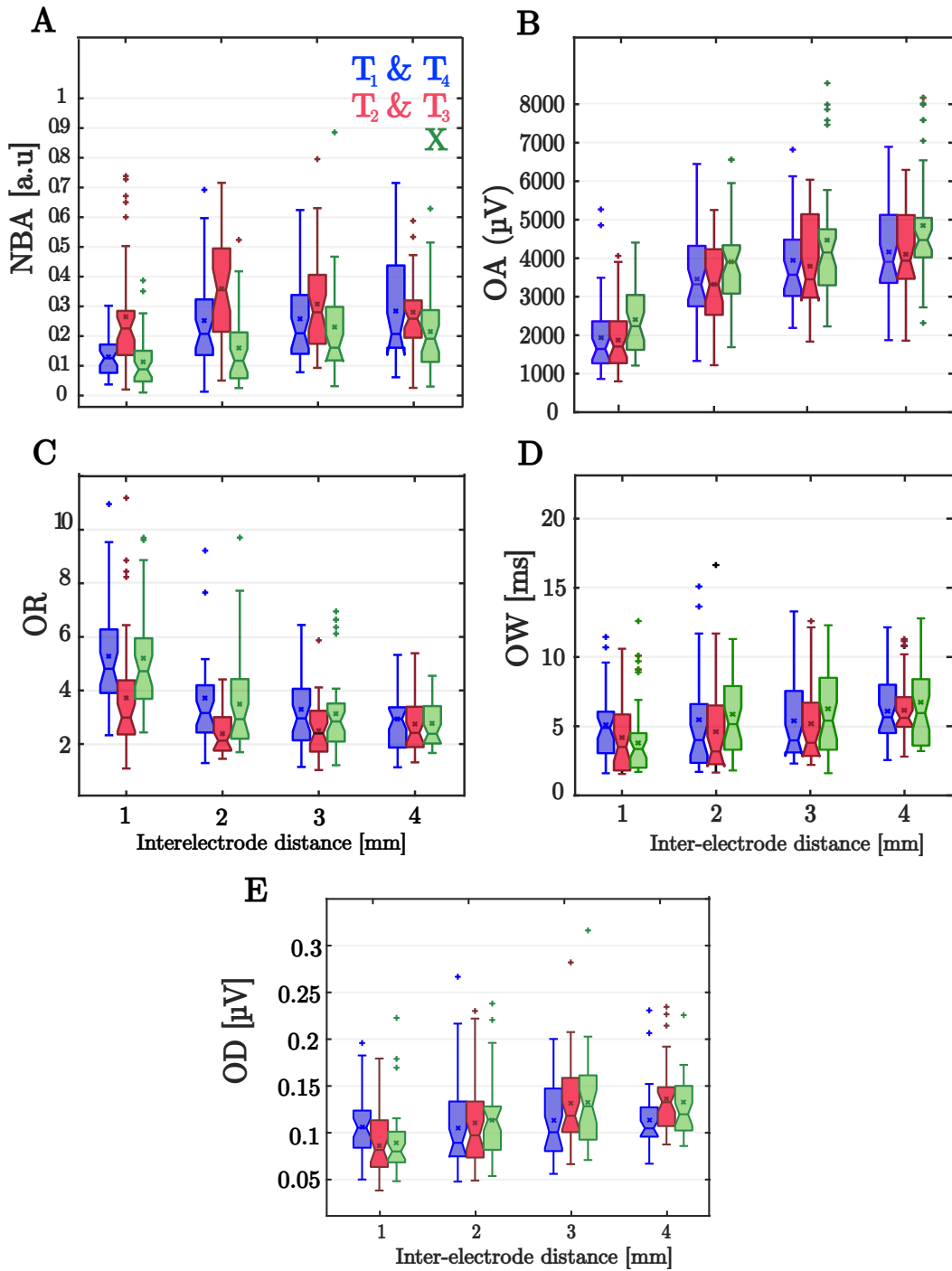


Figure 5.3. Boxplots illustrating the results of the parameters of assessment. A Normalized Bipolar Areas. **B** Amplitude of the θ_x component of omnipoles. **C** Ratio of the θ_x and θ_y omnipolar components. **D** Pulse width of the omnipolar signal (θ_x). **E** Morphological Distortion of the θ_x omnipolar component. Average values from the groups are expressed with 'x' symbol, together with the medians and outliers.

Normalized Bipolar Areas

Starting with the bipolar statistical analysis, the magnitudes of the areas contained within the normalized bipolar loops were analyzed and plotted in the first panel from figure 5.3. Note that the triangular arrangements of complementary geometry were averaged and plotted altogether (in blue for the T_1 and T_4 , and in red for the T_2 and T_3).

In coherence with table 5.1, and the remarks from figures 5.1 and 5.2, the NBA panel illustrates the already mentioned increase in area proportionally to the increase in inter-electrode distance. This is appreciated from the median areas at 1 mm and at 4 mm, where the area values for the three groups increase by a factor of 2.

Observe as well the similarity in the behavior of the triangular configurations T_1 , T_4 to the cross clique.

In the NBA subplot there is a configuration group with clearly larger values of the loop areas, specially for the case $d \leq 2$ mm, corresponding to the triangular cliques T_2 and T_3 .

The statistical evaluation described in section 4.5 confirms all these observations. The fact that the loops retrieved with cross cliques are significantly smaller than those coming from cliques with T_2 and T_3 orientation (for distances ≤ 2 mm); the similarity between triangles T_1 , T_4 and cross (with non significant p-values); and the effect of the electrode spacing, that not only increases the magnitudes of the bEGMs, but also leads to the resemblance in performance between configuration groups (for distances > 2 mm, non significant p-values).

Omnipolar Amplitude

The next panel from figure 5.3 illustrates the increase in omnipolar amplitudes proportionally to the inter-electrode distance already discussed. Notice again how the amplitude is doubled from the 1 mm case, to the 4 mm clique.

It can be also appreciated the similar performance of the triangular arrangements regardless of their geometry, specially when comparing the median of both groups, which are approximately coincident at all distances.

Conversely, the cross group is the one that retrieves the biggest amplitude for the dipoles, with median values superior at all distances.

If we study the statistical evaluation of the results, we can check the validity of the observations performed. In fact, the two triangular groups retrieve non significant p-values at all inter-electrode distances, therewith they hold similar performances. Conversely, the cross configuration is significantly wider in amplitude at $d < 2$ mm.

Omnipolar Ratio

In contrast to the previous case, omnipolar ratios are inversely proportional to the inter-electrode distance. Observe in the next panel (figure 5.3 C) the tendency of the omnipoles.

For distances ≤ 3 mm, the performance of the cross group looks almost identical to that of the triangles T_1 and T_4 . Nonetheless, the group configuration T_2, T_3 , lies below the medians of the other 2 groups, retrieving ratios twice smaller (for the case of 1 mm distance).

The distinction between cross and triangles T_2, T_3 is even clearer if we focus on the significant p-values for distances ≤ 2 mm. The discussed similarity between cross and configurations T_1, T_4 is again remarked in the statistical results, where the non p-values are non significant for all the inter-electrode distances.

Omnipolar Width and Distortion

The last 2 panels from figure 5.3 (D, E), illustrate the dispersion of the magnitudes of omnipolar width and morphological distortion of the omnipoles.

These last parameters do not retrieve any relevant results that might confirm some of the findings just mentioned. However, there is again a visible tendency of the groups, proportional to the increase in electrode spacing. The statistical evaluation shows this distance effect, reflected in the increase in similarity of the groups.

The morphological deviation of the omnipoles with respect to the reference oEGM, $\hat{\Theta}(t)$ is illustrated in figure 5.4. The oEGMs from a particular signal have been normalized and plotted, reconstructed using cliques 1 - 4 mm and a triangular and cross arrangement of the bipolar axes. Despite the temporal misalignment, which was out of the scope of this last analysis, the values of RMSQ of the oEGMs to the $\hat{\Theta}(t)$, was minimum with the cross configuration. The increase in distance leads to an increase in width and fractionation of the signals, specially for the case of T_1 .

5.2.2. Distance effect

To expose the influence of the inter-electrode distance on the quality of the signals, the results from the statistical comparison of particular distance groups have been provided on table 5.3.

For three non-redundant configuration groups (X, average T_1 and T_4 , average T_2 and T_3), every parameter of assessment retrieved from a clique at each inter-electrode distance was compared to the other three distances.

Consequently, the same distance compared to itself yields a p-value of 1 in the diagonal. As the distance difference increases, the statistical similarity decreases, retrieving for instance significant p-values for the case 1 to 4 mm.

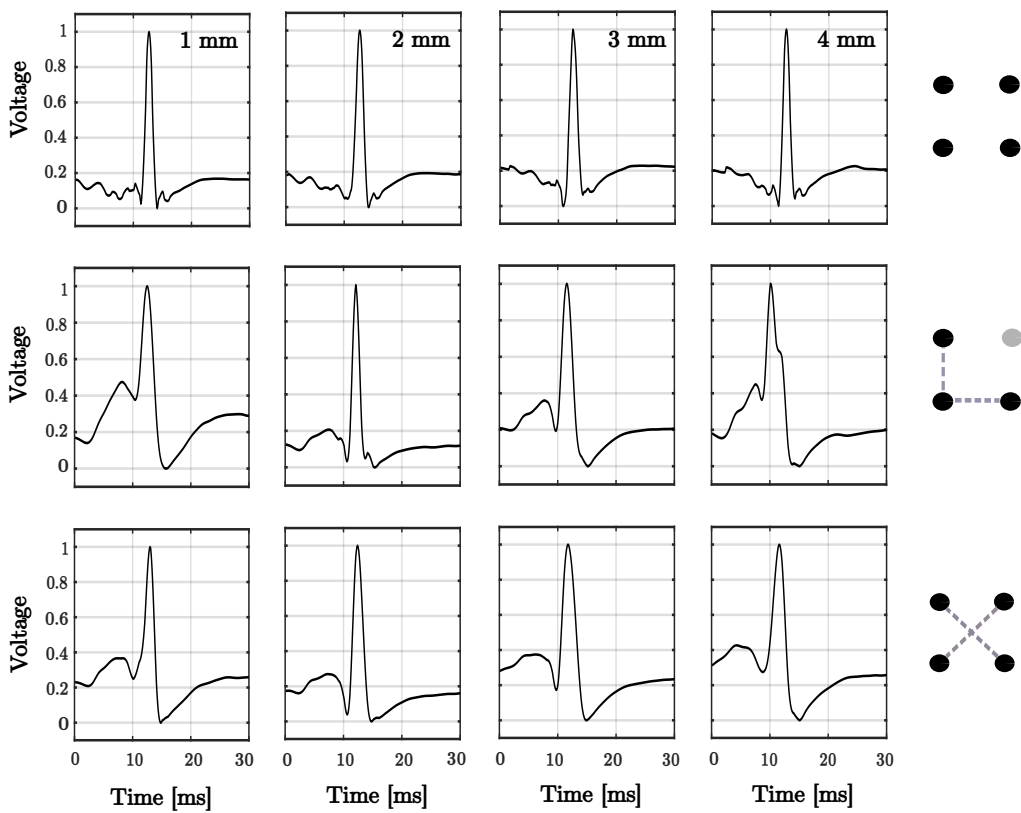


Figure 5.4. Morphology Analysis of the omnipoles. **Top row:** Reference oEGM, $\hat{\Theta}(t)$. **Middle row:** estimated oEGM ($\Theta(t)$) reconstructed using the T_1 clique configuration. **Bottom row:** estimated oEGM ($\Theta(t)$) reconstructed using the cross configuration. A normalization of the voltage amplitudes has been implemented.

	X - T1	X - T2	T1 - T2	X - T1	X - T2	T1 - T2
	Area			Width		
1 mm	0.998	0.0001	0.0046	0.8586	1	0.9576
2 mm	0.79	0.0217	0.812	0.989	0.2767	0.9489
3 mm	0.998	0.79	0.998	0.9511	0.7851	1
4 mm	0.99	0.99	1	0.9961	0.9977	1
	Ratio			Amplitude		
1 mm	1	0.0323	0.0047	0.0936	0.0139	0.9999
2 mm	0.9971	0.0089	0.0002	0.9492	0.4547	0.9991
3 mm	0.9947	0.1034	0.004	0.9906	0.3616	0.9732
4 mm	0.9986	1	0.9965	0.8334	0.561	1
	Distortion					
1 mm	0.8819	0.688	0.6389			
2 mm	1	0.942	1			
3 mm	0.9987	0.999	0.9967			
4 mm	0.9766	0.998	0.9025			

Table 5.2. P-VALUES FOR THE DIFFERENT METRICS OF ASSESSMENT, COMPARING GROUPS TO EACH OTHER

		X				T ₁ & T ₄				T ₂ & T ₃			
		1 mm	2 mm	3 mm	4 mm	1 mm	2 mm	3 mm	4 mm	1 mm	2 mm	3 mm	4 mm
NBA	1 mm	1	0.282	<0.05	<0.05	1	<0.05	<0.05	<0.01	1	0.986	1	1
	2 mm	-	1	0.995	0.810	-	1	1	1	-	1	1	1
	3 mm	-	-	1	1	-	-	1	1	-	-	1	1
	4 mm	-	-	-	1	-	-	-	1	-	-	-	1
OR	1 mm	1	<0.05	<0.001	<0.0001	1	0.057	<0.05	<0.0001	1	<0.01	<0.01	0.121
	2 mm	-	1	0.989	0.239	-	1	0.994	0.203	-	1	1	0.993
	3 mm	-	-	1	0.929	-	-	1	0.872	-	-	1	0.949
	4 mm	-	-	-	1	-	-	-	1	-	-	-	1
OA	1 mm	1	<0.0001	<0.0001	<0.0001	1	<0.0001	<0.0001	<0.0001	1	<0.0001	<0.0001	<0.0001
	2 mm	-	1	0.849	0.171	-	1	0.782	0.319	-	1	0.909	0.120
	3 mm	-	-	1	0.992	-	-	1	1	-	-	1	0.953
	4 mm	-	-	-	1	-	-	-	1	-	-	-	1
OW	1 mm	1	0.072	<0.01	<0.001	1	1	1	0.351	1	1	0.764	<0.01
	2 mm	-	1	1	0.666	-	1	1	0.570	-	1	0.905	<0.05
	3 mm	-	-	1	0.985	-	-	1	0.895	-	-	1	0.629
	4 mm	-	-	-	1	-	-	-	1	-	-	-	1
OD	1 mm	1	0.605	<0.01	<0.01	1	1	0.911	0.947	1	0.708	<0.001	<0.001
	2 mm	-	1	0.669	0.489	-	1	0.833	0.889	-	1	0.238	0.083
	3 mm	-	-	1	1	-	-	1	1	-	-	1	1
	4 mm	-	-	-	1	-	-	-	1	-	-	-	1

Table 5.3. P-VALUES FOR THE METRICS OF ASSESSMENT COMPARING EACH GROUP CLASS

6. DISCUSSION

The technique that tries to overcome the catheter orientation dependency for estimating bipolar electrograms is gaining more and more interest in the cardiac electrophysiology field, it is commonly referred to as OIS (Orientation Independent Sensing) [10].

In fact, the cardiac substrate characterization based on uEGMs is vulnerable to multiple issues already defined, related to noise and far field interferences. bEGMs on the other hand underlie the issue of the orientation dependency on the unpredictable propagation wavefront, resulting in lower amplitudes of the reconstructed signals and a fractionation of the activation pulse. The relevance of working with OIS relies on the need to avoid techniques where the electrode pair orients almost perpendicularly to the propagation wavefront, as low amplitudes and fractionation are keys in the characterization of anomalous conduction regions [67], [68].

For this purpose, several 'orientation-independent' techniques have been developed, raising criticism on whether independency is indeed achieved [11]. In fact, methods for the reconstruction of orientation-independent oEGMs based on triangular arrangements of the cliques, are not fully effective in estimating accurate signals, together with the temporal misalignment with the clique's centroid. Nonetheless, oEGM estimations from the diagonal bipolar axes have proven to be more robust in the oEGM estimation, regardless of the propagation direction and correcting the temporal misalignments [69].

This dissertation attempts to evaluate the effectiveness and constraints of OIS techniques in estimating oEGMs in a practical setting, using a range of retrospective experiments conducted on animal models. Our study tests various technical aspects, including clique configuration and inter-electrode distance, and considers parameters that are based on the form factor of the electric field loop retrieved with the bipolar technology and the quality of the activation pulse derived with the omnipolar technology. Furthermore, we analyze the effect of increasing spacing between electrodes on the distortion of the omnipolar morphology.

It is relevant to highlight the importance of post-processing some of the experimental signals of the study (section 4.3.1), that presented regions of saturation and fractionation. In fact the algorithm proposed for the reconstruction the signals successfully recovers the missing parts, retrieving uEGMs with morphologies extremely natural and accurate, resembling those of real undisturbed uEGMs.

Once the signals were properly corrected, when assessing the optimal clique configuration, it was relevant to recall the fact that the stimulation of the epicardial tissue was performed with an electrode fixed at a constant position in approximately all the experiments, conditioning all the propagation wavefronts to resemble in orientation and morphology (see figure 5.1). Intrinsically related to this biased circumstance of the ex-

periments, is the performance of the triangular arrangements, that varies according to a complementary geometry. Therewith, those triangles whose bisection is parallel to the propagation direction (T_1, T_4) were consistently more accurate. Conversely, the triangular arrangements of orthogonal bisection with respect to the propagation wavefront (T_2, T_3) had a consistently poor performance, with wide electric field loops, and misaligned and wide omnipoles, failing to properly locate the activation site.

Non-withstanding, cross-oriented configurations provided results as precise as the ones from the best complementary triangular pair, with a robust estimation of the propagation wavefront, narrow electric field loops, and precise activation pulses. This was the case when the inter-electrode distance was < 2 mm. Nevertheless, an increase in the clique's size was intrinsically related to computing signals recovered from cells with delays in the activation. This fact lead to difficulties in the interpretation of the results, with signals presenting fractionations and notches, wide bipolar loops and a little distinction between the omnipolar component θ_x and the residual θ_y (figure 5.3).

More particularly for the cross arrangement, there was an additional $\sqrt{2}$ factor when increasing the inter-electrode distance, and therefore the size of the bipolar axes was also increased. For this particular reason, when the distance was ≥ 2 mm, triangular configurations presented bEGMs of comparatively smaller magnitude (regardless of the misalignments with the propagation direction), as well as oEGMs with less fractionated and notched peaks. In fact, due to the diagonal based configuration, the distance increase affected more negatively the cross arrangement. This is a minor issue for a clinical scenario, as the real inter-electrode distance employed in the HD Grid catheter is always smaller than 3 mm [70].

These findings, together with the definition of orientation-independent configuration, make the cross arrangement a promising technique for the reconstruction of activation pulses. The catheter placement within the chamber under study, the direction of the wavefront propagation, or even the possible abnormalities of the arrhythmic tissue to be ablated, are aspects very present in a real-case ablation procedure that can influence the quality of the results retrieved with triangular arrangements.

The cross configuration is robust and insensitive to all these conditions, as we have proven in the previous sections, it is for this reason that the characterization of the cardiac tissue will be eased and refined when introducing this novel technology into the clinical practice.

7. CONCLUSION

In this dissertation project, performances of multiple orientation-independent sensing methods with application on cardiac substrate characterization have been explored. For this purpose, signals recorded from a high-density multielectrode during a retrospective experimental series of isolated perfused rabbit heart were employed.

The first conclusion arising from this dissertation relates to a critic towards the design of electrophysiological catheters commonly used in the clinic, to identify target regions for ablation. In fact, the results indicate that to obtain accurate oEGM estimations, inter-electrode spacing should not exceed 2 mm. This study encourages the design of higher density multi-electrode catheters.

Another point discussed correlates tightly to the configuration method employed to reconstruct signals from the unipolar channels. The findings based on the metrics of assessment of the electric field loops and omnipolar pulses support the hypothesis that, diagonal based bEGMs are more robust and orientation independent than any of the methods previously employed.

Overall, the insights of this thesis provide a standpoint for a more accurate description of the way intracardiac signals are transmitted, with the potential of improving our understanding of the origin of arrhythmias and other severe cardiac diseases. Furthermore, it suggests the possibility of developing new devices and post-processing methods with features to guarantee an improved performance in the cardiovascular procedural surgeries.

8. LIMITATIONS AND FUTURE APPROACHES

This study addresses a hot topic in the field of substrate characterization and electrophysiology, offering a novel reliable method for retrieving cardiac signals from unipolar channels. Although the conclusions derived are solid and in alignment with the hypothesis, there is room for improvement, as the work comes with some limitations that are relevant to be acknowledged.

Starting with the subject of the experiments, therewith rabbit hearts. While animal models can provide valuable insights into human physiology and disease, some of the most relevant limitations when using rabbits instead of humans, are the anatomy and physiologic differences. In fact, rabbit hearts are smaller in size, they have a higher heart rate, different ventricular structure, and different calcium handling, which may affect the experimental results and make it difficult to extrapolate to humans the conclusions derived. There is therefore future work to be performed using the cross-configuration method in cardiac signals coming from human hearts.

Also interesting would be to perform an unbiased experimental study, without post-processing or manipulation of the resulting signals. For this particular project where some signals were futile, it was necessary to implement some kind of reconstruction algorithm for the data-set not to be excessively limited. Nonetheless, future work has to be performed with unsaturated signals, testing the hypothesis of this study.

The fact that electrodes were stimulated using a bipolar catheter located at a fixed position in all the experimental series, also leaves room for criticism. This lead to biased results when considering some triangular arrangements to be invariably more optimal, or consistently unsatisfactory in the detection of the propagation wavefront. Future work could be performed with stimulations at different positions within the cardiac cavity, potentially including pathological cases, for a more unbiased assessment of the robustness of the cross-configuration regardless of the tissue conditions.

Regarding the analytical and methodology stages of this work, there is also room for debate. In fact, we count with a relatively low number of samples, it would be therefore interesting to perform future work with a more objective database, consisting on a multicentric research study, including a broader range of patients from different clinical backgrounds.

9. REGULATORY FRAMEWORK AND SOCIO-ECONOMICAL IMPACT

9.1. Regulatory Frames: Bioethics, Legislation and Licensing

This dissertation work proving several hypothesis has been made possible thanks to the experimental series of studies performed over rabbit hearts.

Animal research has been fundamental in the development of many life-saving drugs and treatments, including vaccines, antibiotics, and cancer therapies [71]. It is however a highly controversial issue, with certain arguing that the use of animals in research is unethical and unnecessary, and that alternative methods should be implemented instead.

In the European Union there is a comprehensive regulatory framework limiting the use of animals in biomedical research. In fact, it is regulated by the Directive 2010/63/EU on the protection of animals employed for scientific purposes [72]. This legislation requires animal experiments to be carried out only when there is no alternative method available, and when the expected benefits of the research justify the use of animals [72].

Regarding the ethics of using animals in biomedical research, it is a topic of greater debate and controversy. Many ethical concerns have been raised, with topics regarding animal welfare, the application of painful or invasive procedures, and the use of animals that are genetically modified or bred specifically for research.

Ethical guidelines have been set requiring animal research protocols to be reviewed and approved by Institutional Animal Care and Use Committees (IACUCs) or similar associations, that animals are housed and cared for in appropriate facilities, and that researchers take steps to minimize animal suffering and distress. These guidelines are based on the 3R's principles, stated by the "Directive on the protection of animals used for scientific purposes" [73]. When conducting any type of animal research, the principle of Replacement must be followed, namely considering that all the possibilities and alternatives to experiment with animals are justifiable only when there is an absence of other options and an imminent necessity. There must be a reduction in the number of animals used for the study, to maintain the scientific quality of the experiments and the relevance of the results (principle of Reduction). The last ethical principle one should account when conducting experiments with animals, is that of Refinement. Researchers must minimize the risk of suffering and provide good animal welfare.

In terms of the protocol followed to register the cardiac signals, the experiments were performed at the Laboratory of experimental Cardiac Electrophysiology at the Department of Physiology of the Polytechnical University of Valencia, through the electrical activity mapping system Maptech, developed in Waalre, the Netherlands.

Regarding software licensing, the main tool employed for the processing and analysis of the signals was Matlab, whose license is covered by the Universidad Carlos III de Madrid. The student had access to a wide range of toolboxes related to signal processing. License free applications were equally used for the editing of all the figures (Inkscape). The statistical analysis of the results, was performed in Rstudio.

9.2. Socio - Economic Impact

9.2.1. Socio-Economic Environment

It is estimated that around 300,000 cardiac events reported every year in the United States, represent 50% of the cardiac deaths [74]. Some of the most common causes of Sudden Cardiac Death (SCD)s are linked to arrhythmogenic cardiomyopathies, the most serious ones including Ventricular Tachycardia (VT) and Ventricular Fibrillation (VF) [75]. Another common type of cardiac arrhythmia, AF is also a condition with significant risk for ischemic stroke, that represents a substantial economic burden as well as morbidity implications [76]. In fact, it is predicted that AF will be affecting between 6-12 million people in the US by 2030 and around 17.9 million people in Europe by 2060.

Estimating the economic burden of cardiomyopathies is a tough subject, there are a wide number of pathologically different cardiac conditions, where the diagnosis and treatment might vary across countries as the Healthcare system will differ.

According to a study published by the Journal of the American Heart Association in 2018 [77], the total direct medical costs associated with ventricular arrhythmias (including VT and VF) in the US was estimated to be \$ 2.2 billion per year. This cost breakdown includes hospitalizations, diagnostic testing, procedures and medication.

The idea of reducing these expenses can be targeted by means of multiple approaches. Improving the accuracy and robustness in the detection algorithms employed for locating cardiac ablation sources, is one feasible approach.

The novel crossed-electrode arrangement optimization technique, that can be implemented to the software compatible with the electro-anatomical catheters used in common cardiac ablation procedures, can improve the results derived from other conventional approaches, as it becomes a very robust and accurate characterization algorithm, that allows for considerable amount of time and money to be saved.

9.2.2. Project resources and Costs

The invested time and funds for the development of this project are exposed in this section.

Table 9.1 summarizes the main personnel required for the development of this dissertation, which was coordinated by two professors from the Polytechnical University of Valencia and closely supervised by an associate researcher collaborator at UPV and Master student at ETH, Zürich. For the statistical section, the help of a PhD student at ETH Zürich, with expertise in advanced statistical modelling was required. Additionally, two cardiologists were needed for the reviewing process of the article derived from this work (see Appendix).

The approximated salaries and invested number of working hours has been estimated making use of the data from Instituto Nacional de Estadística (National Institute of Statistics) [78].

	Time invested (h)	Cost/time (€/h)	Total cost (€)
Student	1200	10	14400
UC3M Advisor	30	40	900
Principal Investigators (x2)	100	40	6000
MSc student advisor	120	20	2040
Cardiologists (x2)	5	60	600
PhD student advisor	20	25	500
	Total		24440

Table 9.1. HUMAN RESOURCES BREAKDOWN

The materials required for the development of this work are summarized on table 9.2. A high computational component was required for the design of the project, therefore the economical burden implied in material resources was not too large.

	Cost/unit (€)	Time Invested (Years)	Total cost (€)
Personal Computer	900	1	900
Screen	200	1	200
Computer accessories	100	1	100
MS office 2016	140	1	140
Matlab Software R2022a	250	1	250
Maptech software	-	-	-
	Total		1590

Table 9.2. MATERIAL RESOURCES BREAKDOWN

During the developmental stage of this dissertation, some of the preliminary results were included in a brief article that was presented at the XL edition of the CASEIB (National Biomedical Engineering Congress), hosted at the University of Valladolid (see Appendix). The complete research team participated in this congress, therefore, the total

costs of participation, accommodation and expenditure for this congress are summarized in table 9.3.

Resources for CASEIB congress		
Object	Cost/Person (€)	Total Cost (€)
Congress Presenter (x2 students)	250	500
Congress Presenter (x1 Professor)	250	250
Congress Presenter (x1 MSc student)	250	250
Travel costs (x4)	70	280
Accommodation (x4)	80	320
Total		1600

Table 9.3. ATTENDANCE TO CASEIB CONGRESS

Overall, taking into account the total costs for human and material resources as well as the expenses for the CASEIB congress are summarized in table 9.4. In total, this project is estimated to be 27630 €.

Type of Resource	Cost(€)
Human	24440
Material	1590
Congresses	1600
Total	27630

Table 9.4. TOTAL COST BREAKDOWN

BIBLIOGRAPHY

- [1] E. Yilmaz, “An expert system based on fisher score and ls-svm for cardiac arrhythmia diagnosis,” *Computational and mathematical methods in medicine*, vol. 2013, 2013.
- [2] M. T. Keating and M. C. Sanguinetti, “Molecular and cellular mechanisms of cardiac arrhythmias,” *Cell*, vol. 104, no. 4, pp. 569–580, 2001.
- [3] L. Gaztañaga, F. E. Marchlinski, and B. P. Betensky, “Mechanisms of cardiac arrhythmias,” *Revista Española de Cardiología (English Edition)*, vol. 65, no. 2, pp. 174–185, 2012.
- [4] N. Akoum and N. Marrouche, “Assessment and impact of cardiac fibrosis on atrial fibrillation,” *Current cardiology reports*, vol. 16, no. 8, pp. 1–7, 2014.
- [5] N. F. Marrouche *et al.*, “Association of atrial tissue fibrosis identified by delayed enhancement mri and atrial fibrillation catheter ablation: The decaaf study,” *Jama*, vol. 311, no. 5, pp. 498–506, 2014.
- [6] B. Bellmann *et al.*, “First epicardial mapping of the left ventricle using the advisor™ hd grid catheter,” *journal of Interventional Cardiac Electrophysiology*, vol. 53, no. 1, pp. 103–104, 2018.
- [7] K. L. Hong *et al.*, “High-resolution mapping of the atria using the hd grid catheter,” *HeartRhythm Case Reports*, vol. 5, no. 7, pp. 351–353, 2019.
- [8] A. Porta-Sanchez *et al.*, “Omnipolarity applied to equi-spaced electrode array for ventricular tachycardia substrate mapping,” *EP Europace*, vol. 21, no. 5, pp. 813–821, 2019.
- [9] R. Jiang *et al.*, “High-density grid catheter for detailed mapping of sinus rhythm and scar-related ventricular tachycardia: Comparison with a linear duodecapolar catheter,” *Clinical Electrophysiology*, vol. 6, no. 3, pp. 311–323, 2020.
- [10] D. C. Deno *et al.*, “Orientation-independent catheter-based characterization of myocardial activation,” *IEEE transactions on biomedical engineering*, vol. 64, no. 5, pp. 1067–1077, 2016.
- [11] J. Riccio *et al.*, “Characterization of atrial propagation patterns and fibrotic substrate with a modified omnipolar electrogram strategy in multi-electrode arrays,” *Frontiers in Physiology*, vol. 12, 2021.
- [12] A. Noordergraaf. Elsevier, 2012, vol. 1.
- [13] J. E. Hall and M. E. Hall, *Guyton and Hall textbook of medical physiology e-Book*. Elsevier Health Sciences, 2020.
- [14] J. P. Holt, “The normal pericardium,” *The American journal of cardiology*, vol. 26, no. 5, pp. 455–465, 1970.

- [15] R. Shabetai, *The pericardium*. Springer Science & Business Media, 2003, vol. 249.
- [16] K. Vogiatzidis *et al.*, “Physiology of pericardial fluid production and drainage,” *Frontiers in physiology*, vol. 6, p. 62, 2015.
- [17] G. J. Tortora and B. H. Derrickson, *Principles of anatomy and physiology*. John Wiley & Sons, 2018.
- [18] J. D. Pollock and A. N. Makaryus, “Physiology, cardiac cycle,” in *StatPearls [Internet]*, StatPearls Publishing, 2022.
- [19] D. S. Park and G. I. Fishman, “The cardiac conduction system,” *Circulation*, vol. 123, no. 8, pp. 904–915, 2011.
- [20] C. W. Lo, *Role of gap junctions in cardiac conduction and development: Insights from the connexin knockout mice*, 2000.
- [21] A. J. Vander *et al.* McGraw-Hill New York, 1990.
- [22] D. W. Whalley, D. J. Wendt, and A. O. Grant, “Basic concepts in cellular cardiac electrophysiology: Part i: Ion channels, membrane currents, and the action potential,” *Pacing and Clinical Electrophysiology*, vol. 18, no. 8, pp. 1556–1574, 1995.
- [23] R. H. Clayton, “Computational models of normal and abnormal action potential propagation in cardiac tissue: Linking experimental and clinical cardiology,” *Physiological Measurement*, vol. 22, no. 3, R15, 2001.
- [24] R. H. Anderson *et al.*, “The anatomy of the cardiac conduction system,” *Clinical Anatomy: The Official journal of the American Association of Clinical Anatomists and the British Association of Clinical Anatomists*, vol. 22, no. 1, pp. 99–113, 2009.
- [25] R. A. Kelly and T. W. Smith, “Cytokines and cardiac contractile function,” *Circulation*, vol. 95, no. 4, pp. 778–781, 1997.
- [26] H. Fukuta and W. C. Little, “The cardiac cycle and the physiologic basis of left ventricular contraction, ejection, relaxation, and filling,” *Heart failure clinics*, vol. 4, no. 1, pp. 1–11, 2008.
- [27] L. Q. Liang *et al.*, “Development of heart simulator (heart-s) on the left ventricle for measuring the blood circulation during cardiac cycle,” in *Journal of Biomimetics, Biomaterials and Biomedical Engineering*, Trans Tech Publ, vol. 36, 2018, pp. 78–83.
- [28] C. S. Peskin, “Fluid dynamics of the heart and its valves,” in *APS Division of Fluid Dynamics Meeting Abstracts*, 1997, 3INV–02.
- [29] D. B. Geselowitz, “On the theory of the electrocardiogram,” *Proceedings of the IEEE*, vol. 77, no. 6, pp. 857–876, 1989.
- [30] S. Sossalla and D. Vollmann, “Arrhythmia-induced cardiomyopathy: Causes, clinical significance, and treatment,” *Deutsches Ärzteblatt International*, vol. 115, no. 19, p. 335, 2018.

- [31] F. H. Fenton, E. M. Cherry, and L. Glass, “Cardiac arrhythmia,” *Scholarpedia*, vol. 3, no. 7, p. 1665, 2008.
- [32] F. Ye *et al.*, “The clinical significance of relative bradycardia.,” *WMJ: official publication of the State Medical Society of Wisconsin*, vol. 117, no. 2, pp. 73–78, 2018.
- [33] A.-E. Baruteau *et al.*, “Evaluation and management of bradycardia in neonates and children,” *European journal of pediatrics*, vol. 175, no. 2, pp. 151–161, 2016.
- [34] J. M. Mangrum and J. P. DiMarco, “The evaluation and management of bradycardia,” *New England journal of Medicine*, vol. 342, no. 10, pp. 703–709, 2000.
- [35] J. S. Shinbane *et al.*, “Tachycardia-induced cardiomyopathy: A review of animal models and clinical studies,” *journal of the American College of Cardiology*, vol. 29, no. 4, pp. 709–715, 1997.
- [36] R. A. Gray *et al.*, “Mechanisms of cardiac fibrillation,” *Science*, vol. 270, no. 5239, pp. 1222–1223, 1995.
- [37] M. Vaquero, D. Calvo, and J. Jalife, “Cardiac fibrillation: From ion channels to rotors in the human heart,” *Heart rhythm*, vol. 5, no. 6, pp. 872–879, 2008.
- [38] B. Swynghedauw, “Molecular mechanisms of myocardial remodeling,” *Physiological reviews*, vol. 79, no. 1, pp. 215–262, 1999.
- [39] T. A. Wynn, “Fibrotic disease and the th1/th2 paradigm,” *Nature Reviews Immunology*, vol. 4, no. 8, pp. 583–594, 2004.
- [40] T. Wynn, “Cellular and molecular mechanisms of fibrosis,” *The journal of Pathology: A journal of the Pathological Society of Great Britain and Ireland*, vol. 214, no. 2, pp. 199–210, 2008.
- [41] S. Hinderer and K. Schenke-Layland, “Cardiac fibrosis—a short review of causes and therapeutic strategies,” *Advanced drug delivery reviews*, vol. 146, pp. 77–82, 2019.
- [42] R.-J. Lin *et al.*, “Role of circulating fibrocytes in cardiac fibrosis,” *Chinese Medical journal*, vol. 129, no. 03, pp. 326–331, 2016.
- [43] C. Antzelevitch, “Basic mechanisms of reentrant arrhythmias,” *Current opinion in cardiology*, vol. 16, no. 1, pp. 1–7, 2001.
- [44] T.-J. Wu *et al.*, “Characteristics of wave fronts during ventricular fibrillation in human hearts with dilated cardiomyopathy: Role of increased fibrosis in the generation of reentry,” *Journal of the American College of Cardiology*, vol. 32, no. 1, pp. 187–196, 1998.
- [45] D. L. Packer *et al.*, “Catheter ablation versus antiarrhythmic drug therapy for atrial fibrillation (cabana) trial: Study rationale and design,” *American heart journal*, vol. 199, pp. 192–199, 2018.

- [46] P. Della Bella *et al.*, “Image integration-guided catheter ablation of atrial fibrillation: A prospective randomized study,” *journal of cardiovascular electrophysiology*, vol. 20, no. 3, pp. 258–265, 2009.
- [47] H. Calkins *et al.*, “Hrs/ehra/ecas expert consensus statement on catheter and surgical ablation of atrial fibrillation: Recommendations for personnel, policy, procedures and follow-up,” *Europace*, vol. 9, no. 6, pp. 335–379, 2007.
- [48] L. Fiedler *et al.*, “Characterization of high-density mapping in catheter ablation for persistent atrial fibrillation: Results from the advisor™ hd grid mapping catheter observational study,” *journal of Interventional Cardiac Electrophysiology*, pp. 1–11, 2022.
- [49] B. Verma *et al.*, “Regional conduction velocity calculation from clinical multichannel electrograms in human atria,” *Computers in biology and medicine*, vol. 92, pp. 188–196, 2018.
- [50] W. G. Stevenson and K. Soejima, “Recording techniques for clinical electrophysiology,” *journal of cardiovascular electrophysiology*, vol. 16, no. 9, pp. 1017–1022, 2005.
- [51] L. J. van der Does and N. M. de Groot, “Inhomogeneity and complexity in defining fractionated electrograms,” *Heart rhythm*, vol. 14, no. 4, pp. 616–624, 2017.
- [52] S. M. Blanchard *et al.*, “The effects of distant cardiac electrical events on local activation in unipolar epicardial electrograms,” *IEEE transactions on biomedical engineering*, no. 7, pp. 539–546, 1987.
- [53] M. Takigawa *et al.*, “Impact of spacing and orientation on the scar threshold with a high-density grid catheter,” *Circulation: Arrhythmia and Electrophysiology*, vol. 12, no. 9, e007158, 2019.
- [54] M. Rillo *et al.*, “A new interpretation of nonpulmonary vein substrates of the left atrium in patients with atrial fibrillation,” *journal of Arrhythmia*, vol. 37, no. 2, pp. 338–347, 2021.
- [55] I. Sim *et al.*, “Left atrial voltage mapping: Defining and targeting the atrial fibrillation substrate,” *journal of Interventional Cardiac Electrophysiology*, vol. 56, no. 3, pp. 213–227, 2019.
- [56] M. S. van Schie *et al.*, “Identification of low-voltage areas: A unipolar, bipolar, and omnipolar perspective,” *Circulation: Arrhythmia and Electrophysiology*, vol. 14, no. 7, e009912, 2021.
- [57] A. Guill *et al.*, “Epicardial-limited electrophysiological heterogeneities do not facilitate ventricular arrhythmia induction. an experimental study,” IEEE, 2015, pp. 701–704.
- [58] A. Friedman, *Advanced calculus*. Courier Corporation, 2012.
- [59] P. McCullagh, “What is a statistical model?” *The Annals of Statistics*, vol. 30, no. 5, pp. 1225–1310, 2002.

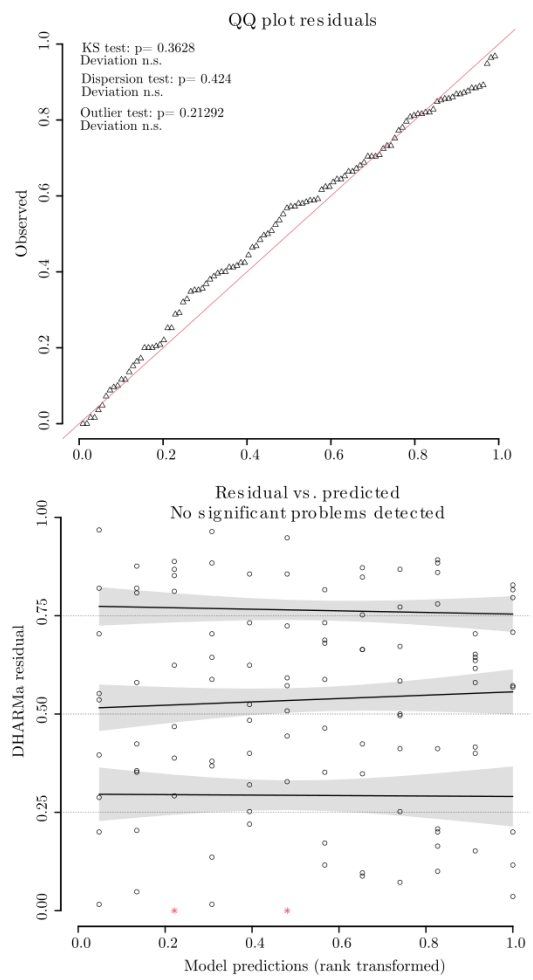
- [60] V. W. Berger and Y. Zhou, “Kolmogorov–smirnov test: Overview,” 2014.
- [61] P. E. McKnight and J. Najab, “Mann-whitney u test,” *The Corsini encyclopedia of psychology*, pp. 1–1, 2010.
- [62] J. Fox, *Applied regression analysis and generalized linear models*. Sage Publications, 2015.
- [63] D. Bates *et al.*, “Fitting linear mixed models in r,” *R news*, vol. 5, no. 1, pp. 27–30, 2005.
- [64] J. C. Gardiner, Z. Luo, and L. A. Roman, “Fixed effects, random effects and gee: What are the differences?” *Statistics in medicine*, vol. 28, no. 2, pp. 221–239, 2009.
- [65] K. Kim and G. Shevlyakov, “Why gaussianity?” *IEEE Signal Processing Magazine*, vol. 25, no. 2, pp. 102–113, 2008.
- [66] K. Yang, J. Tu, and T. Chen, “Homoscedasticity: An overlooked critical assumption for linear regression,” *General psychiatry*, vol. 32, no. 5, 2019.
- [67] J. M. De Bakker and F. H. Wittkampf, “The pathophysiologic basis of fractionated and complex electrograms and the impact of recording techniques on their detection and interpretation,” *Circulation: Arrhythmia and Electrophysiology*, vol. 3, no. 2, pp. 204–213, 2010.
- [68] A. S. Jadidi *et al.*, “Functional nature of electrogram fractionation demonstrated by left atrial high-density mapping,” *Circulation: Arrhythmia and Electrophysiology*, vol. 5, no. 1, pp. 32–42, 2012.
- [69] F. Castells *et al.*, “Performance assessment of electrode configurations for the estimation of omnipolar electrograms from high density arrays,” *Computers in Biology and Medicine*, vol. 154, p. 106 604, 2023.
- [70] D. R. Frisch, “Identifying a gap in a cavotricuspid isthmus flutter line using the advisor™ hd grid high-density mapping catheter,” *The journal of Innovations in Cardiac Rhythm Management*, vol. 10, no. 12, p. 3919, 2019.
- [71] A. R. Giles *et al.*, “Guidelines for the use of animals in biomedical research,” *Thrombosis and haemostasis*, vol. 58, no. 08, pp. 1078–1084, 1987.
- [72] A. V. Sykes *et al.*, “Directive 2010/63/eu on animal welfare: A review on the existing scientific knowledge and implications in cephalopod aquaculture research,” *Reviews in Aquaculture*, vol. 4, no. 3, pp. 142–162, 2012.
- [73] S. Louhimies, “Directive 86/609/eec on the protection of animals used for experimental and other scientific purposes,” *Alternatives to Laboratory Animals*, vol. 30, no. 2_suppl, pp. 217–219, 2002.
- [74] R. J. Myerburg, K. M. Kessler, and A. Castellanos, “Sudden cardiac death: Epidemiology, transient risk, and intervention assessment,” *Annals of internal medicine*, vol. 119, no. 12, pp. 1187–1197, 1993.
- [75] R. J. Myerburg, “Cardiac arrest and sudden cardiac death,” *Heart disease*, 2001.

- [76] G. Lippi, F. Sanchis-Gomar, and G. Cervellin, “Global epidemiology of atrial fibrillation: An increasing epidemic and public health challenge,” *International journal of Stroke*, vol. 16, no. 2, pp. 217–221, 2021.
- [77] E. J. Benjamin *et al.*, “Heart disease and stroke statistics—2018 update: A report from the american heart association,” *Circulation*, vol. 137, no. 12, e67–e492, 2018.
- [78] *Instituto Nacional de Estadística*, <https://www.ine.es/>, Accessed: 02-06-2023.
- [79] M. C. Aguirre *et al.*, “Estudio comparativo con señales epicárdicas de las limitaciones del omnipolo con multielectrodos de alta densidad,”

APPENDIX A

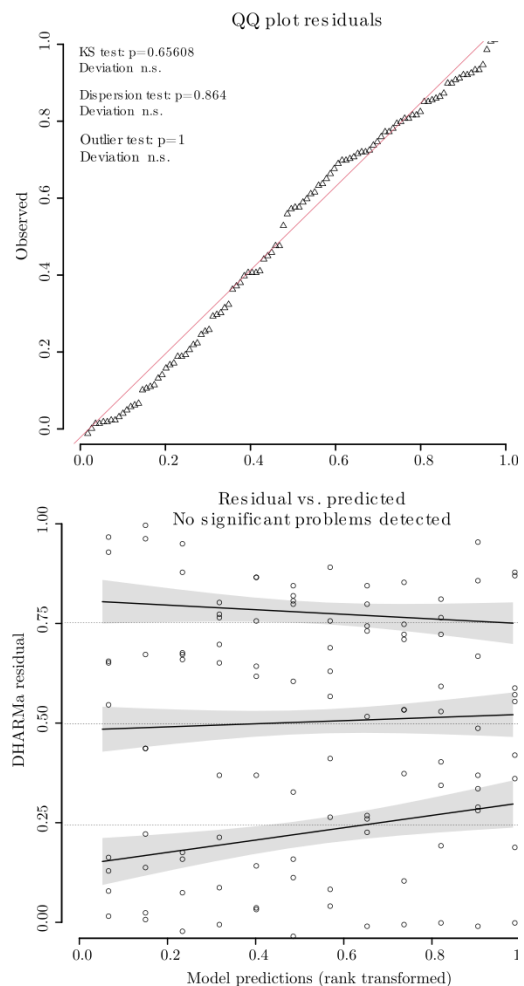
A.1 Statistical model : NBA

Predictors	log(NBA)		
	Estimates	CI	p
(Intercept)	-2.20	-2.43 – -1.98	<0.001
configuration [T2]	0.65	0.34 – 0.96	<0.001
configuration [X]	-0.15	-0.46 – 0.17	0.353
distance [2mm]	0.55	0.24 – 0.87	0.001
distance [3mm]	0.58	0.27 – 0.89	<0.001
distance [4mm]	0.66	0.34 – 0.97	<0.001
configuration [T2] × distance [2mm]	-0.36	-0.81 – 0.08	0.105
configuration [X] × distance [2mm]	-0.14	-0.58 – 0.30	0.524
configuration [T2] × distance [3mm]	-0.50	-0.94 – -0.06	0.026
configuration [X] × distance [3mm]	0.00	-0.44 – 0.44	0.989
configuration [T2] × distance [4mm]	-0.57	-1.01 – -0.13	0.012
configuration [X] × distance [4mm]	0.04	-0.40 – 0.48	0.856
Random Effects			
σ^2	0.11		
τ_{00} rabbit	0.00		
ICC	0.03		
N rabbit	9		
Observations	108		
Marginal R ² / Conditional R ²	0.423 / 0.442		



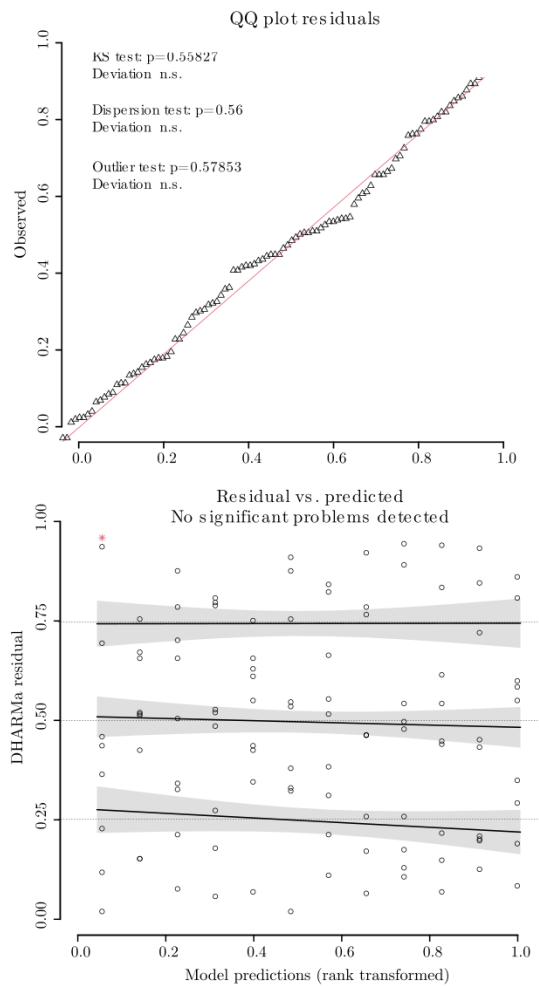
A.2 Statistical model : OA

Predictors	log(OA)		
	Estimates	CI	p
(Intercept)	7.58	7.38 – 7.78	<0.001
configuration [T2]	-0.04	-0.16 – 0.08	0.508
configuration [X]	0.19	0.07 – 0.31	0.002
distance [2mm]	0.56	0.44 – 0.68	<0.001
distance [3mm]	0.68	0.55 – 0.80	<0.001
distance [4mm]	0.72	0.60 – 0.84	<0.001
configuration [T2] × distance [2mm]	-0.01	-0.19 – 0.16	0.873
configuration [X] × distance [2mm]	-0.10	-0.27 – 0.07	0.241
configuration [T2] × distance [3mm]	-0.03	-0.20 – 0.14	0.727
configuration [X] × distance [3mm]	-0.11	-0.28 – 0.06	0.208
configuration [T2] × distance [4mm]	0.01	-0.16 – 0.19	0.868
configuration [X] × distance [4mm]	-0.08	-0.25 – 0.09	0.339
Random Effects			
σ^2	0.02		
τ_{00} rabbit	0.07		
ICC	0.81		
N rabbit	9		
Observations	108		
Marginal R ² / Conditional R ²	0.477 / 0.901		



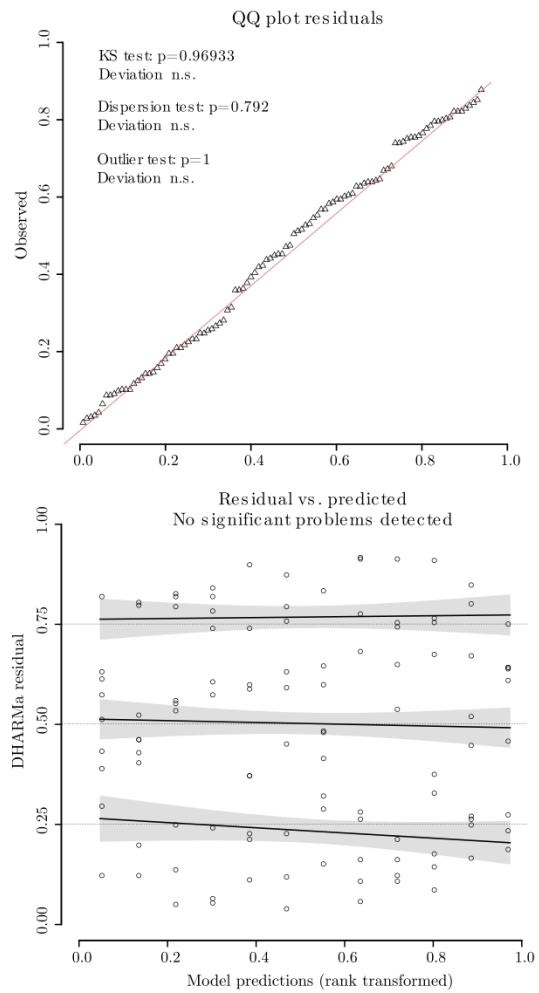
A.3 Statistical model : OR

Predictors	log(OR)		
	Estimates	CI	p
(Intercept)	1.70	1.54 – 1.86	<0.001
configuration [T2]	-0.42	-0.62 – -0.22	<0.001
configuration [X]	-0.06	-0.26 – 0.14	0.547
distance [2mm]	-0.34	-0.54 – -0.13	0.001
distance [3mm]	-0.45	-0.65 – -0.25	<0.001
distance [4mm]	-0.62	-0.82 – -0.42	<0.001
configuration [T2] × distance [2mm]	-0.08	-0.37 – 0.20	0.564
configuration [X] × distance [2mm]	-0.04	-0.33 – 0.24	0.775
configuration [T2] × distance [3mm]	-0.01	-0.29 – 0.28	0.972
configuration [X] × distance [3mm]	-0.05	-0.33 – 0.24	0.736
configuration [T2] × distance [4mm]	0.31	0.03 – 0.60	0.032
configuration [X] × distance [4mm]	-0.03	-0.32 – 0.25	0.819
Random Effects			
σ^2	0.05		
τ_{00} rabbit	0.01		
ICC	0.19		
N _{rabbit}	9		
Observations	108		
Marginal R ² / Conditional R ²	0.556 / 0.638		



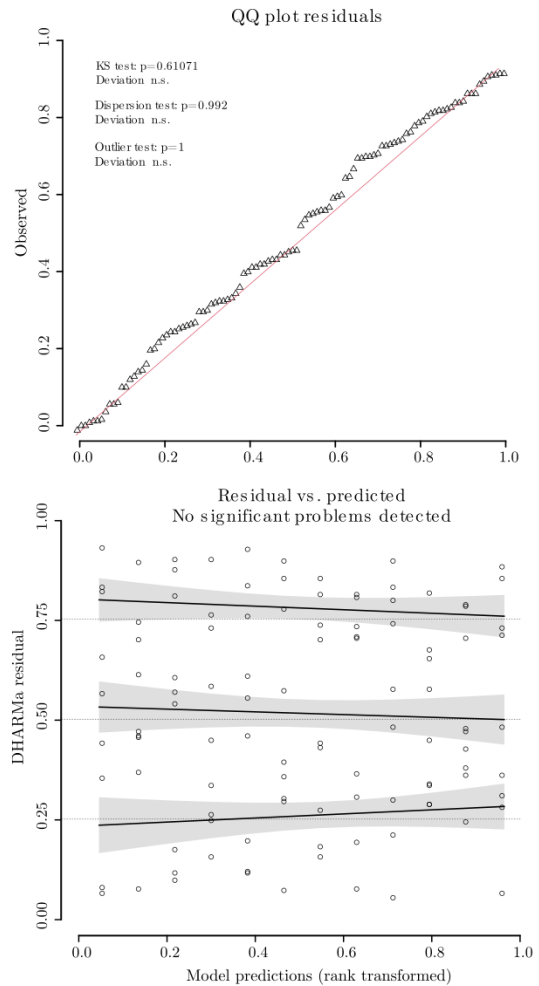
A.4 Statistical model : OD

Predictors	log(OD)		
	Estimates	CI	p
(Intercept)	-2.32	-2.46 – -2.18	<0.001
configuration [T2]	-0.17	-0.33 – -0.01	0.040
configuration [X]	-0.14	-0.30 – -0.03	0.101
distance [2mm]	-0.01	-0.18 – 0.15	0.857
distance [3mm]	0.13	-0.03 – 0.29	0.117
distance [4mm]	0.12	-0.04 – 0.28	0.148
configuration [T2] × distance [2mm]	0.18	-0.05 – 0.41	0.131
configuration [X] × distance [2mm]	0.19	-0.04 – 0.42	0.106
configuration [T2] × distance [3mm]	0.25	0.02 – 0.49	0.031
configuration [X] × distance [3mm]	0.21	-0.02 – 0.44	0.071
configuration [T2] × distance [4mm]	0.30	0.07 – 0.53	0.011
configuration [X] × distance [4mm]	0.24	0.01 – 0.47	0.039
Random Effects			
σ^2	0.03		
τ_{00} rabbit	0.02		
ICC	0.35		
N _{rabbit}	9		
Observations	108		
Marginal R ² / Conditional R ²	0.288 / 0.534		



A.5 Statistical model : OW

Predictors	log(OD)		
	Estimates	CI	p
(Intercept)	3.85	3.62 – 4.07	<0.001
configuration [T2]	-0.15	-0.36 – 0.06	0.161
configuration [X]	-0.18	-0.39 – 0.03	0.090
distance [2mm]	0.03	-0.18 – 0.25	0.743
distance [3mm]	0.09	-0.12 – 0.30	0.381
distance [4mm]	0.27	0.06 – 0.48	0.014
configuration [T2] × distance [2mm]	-0.00	-0.30 – 0.29	0.978
configuration [X] × distance [2mm]	0.31	0.01 – 0.60	0.044
configuration [T2] × distance [3mm]	0.11	-0.19 – 0.40	0.478
configuration [X] × distance [3mm]	0.33	0.04 – 0.63	0.028
configuration [T2] × distance [4mm]	0.16	-0.14 – 0.45	0.300
configuration [X] × distance [4mm]	0.29	-0.01 – 0.59	0.054
Random Effects			
σ^2	0.05		
τ_{00} rabbit	0.06		
ICC	0.56		
N rabbit	9		
Observations	108		
Marginal R ² / Conditional R ²	0.211 / 0.651		



APPENDIX B

Publications derived from this dissertation thesis

M. Crespo Aguirre et al. "Estudio comparativo con señales epicárdicas de las limitaciones del omnípolo con multielectrodos de alta densidad". Work submitted to Congreso Anual de la Sociedad Española de Ingeniería Biomédica. Valladolid November 2022. [79]